Sea-ice drag as a function of deformation and ice cover: Effects on simulated sea ice and ocean circulation in the Arctic.

GIULIA CASTELLANI[a,*], Martin Losch[a], Mischa Ungermann[a], Rüdiger Gerdes[a]

[a] *Alfred Wegener Institute Helmholtz Centre for Polar and Marine Research, Am Handelshafen 12, D-27570 Bremerhaven, Germany.*

Abstract

Many state-of-the-art coupled sea ice-ocean models use atmospheric and oceanic drag coefficients that are at best a function of the atmospheric stability but otherwise constant in time and space. Constant drag coefficients might lead to an incorrect representation of the ice-air and ice-ocean momentum exchange, since observations of turbulent fluxes imply high variability of drag coefficients. We compare three model runs, two with constant drag coefficients and one with drag coefficients varying as function of sea-ice characteristics. The computed drag coefficients range between 0.88 $\times 10^{-3}$ and 4.68 $\times 10^{-3}$ for the atmosphere, and between 1.28 $\times 10^{-3}$ and 13.68 $\times 10^{-3}$ for the ocean. They fall in the range of observed drag coefficients and illustrate the interplay of ice deformation and ice concentration in different seasons and regions. The introduction of variable drag coefficients improves the realism of the model simulation. In addition, using the average values of the variable drag coefficients improves simulations with constant drag coefficients. When drag coefficients depend on sea-ice characteristics, the average sea-ice drift speed in the Arctic basin increases from 6.22 cm s^{-1} to 6.64 cm s^{-1}. This leads to a reduction of ice thickness in the entire Arctic and particularly in the Lincoln Sea with a mean value decreasing from 7.86 m to 6.62 m. Variable drag coefficients lead also to a deeper mixed layer in summer

*Corresponding author. *E-mail address:* giulia.castellani@awi.de

and to changes in surface salinity. Surface temperatures in the ocean are also affected by variable drag coefficients with differences of up to 0.06°C in the East Siberian Sea. Small effects are visible in the ocean interior

1. Introduction

The recently observed changes in Arctic sea ice (Rothrock et al., 1999; Serreze et al., 2003, 2007; Stroeve et al., 2007, 2012a,b; Laxon et al., 2013; Haas et al., 2008; Rabenstein et al., 2010; Castellani et al., 2014) feed back into the global climate because sea ice is coupled to atmosphere and oceans. Sea ice insulates the oceans from the polar atmosphere, it contributes to the ice-albedo feedback mechanism (Curry et al., 1995), and, while drifting, it exerts a drag on the oceanic surface layer. This drag fluxes momentum into the ocean. The momentum fluxes between ice and ocean affect the upper surface circulation with consequences for the interior ocean circulation and the outflow into the Nordic Seas as well as the Pacific and Atlantic Ocean (Proshutinsky & Johnson, 1997; Rudels et al., 2005; Latarius & Quadfasel, 2010; Proshutinsky et al., 2009). Understanding the dynamic coupling between ice, atmosphere and ocean requires a detailed representation of the momentum fluxes.

In this work, we aim to contribute to improving the representation of physical processes in coupled sea-ice–ocean models by investigating how numerical simulations are affected by a description of ice-atmosphere and ice-ocean coupling that accounts for the sea-ice roughness.

Most sea-ice codes resolve both dynamic and thermodynamic processes. The sea-ice momentum equations are solved for drift velocities that are then used to advect the ice variables. The drift velocities also determine the stress acting on the ocean. In most sea-ice models (Hibler, 1979; Hunke, 2010), both the atmospheric drag and the oceanic drag are described by a quadratic relationship (see also the Arctic Ocean Model Intercomparison Project -AOMIP- protocol, Proshutinsky et al., 2001) depending on the relative velocity between atmospheric wind (ocean currents) and sea-ice drift. The intensity of the air-ice

and ocean-ice interactions are described by the transfer coefficients called air drag coefficient c_a and ocean drag coefficient c_w. These coefficients depend on sea-ice surface characteristics. Table 1 lists direct observations of atmospheric drag coefficients and indirect estimates from linear (Castellani et al., 2014) and 3D (Petty et al., 2017) surface profiles, all at a reference height of 10 m; and oceanic drag coefficients that are generally referenced to geostrophic currents (Lu et al., 2011).

Many sea-ice models in coupled GCMs today use constant drag coefficients, thus they do not account for their observed spatial and temporal variability (Hunke et al., 2010). In recent years many parameterizations have been developed to relate sea-ice surface characteristics to drag coefficients (Garbrecht et al., 2002; Birnbaum & Luepkes, 2002; Lüpkes & Birnbaum, 2005; Lüpkes et al., 2012, 2013; Andreas et al., 2010; Lu et al., 2011), and some of these parameterizations have been implemented in numerical models. For example, Tsamados et al. (2014) present the results of a simulation with the Los Alamos sea-ice model CICE where some of the mentioned parameterizations are used to compute the atmospheric and oceanic neutral drag coefficients as a function of floe edges, ridges, and melt ponds. Moreover, CICE allows to include instability effects of the surface layer over sea ice, thus the neutral drag coefficients are corrected for the stability that depends on the thickness distribution and thus on the sea-ice surface state (Hunke et al., 2015). The approach of Tsamados et al. (2014) requires a dynamic ice thickness distribution (ITD) as well as an explicit description of ridges and melt ponds formation (Flocco & Felthman, 2007; Flocco et al., 2010). In a different approach (Steiner et al., 1999; Steiner, 2001), deformation energy accounts for surface roughness. The deformation energy depends on the history of the mechanical deformation of sea ice and on changes in its thickness. The drag coefficients are parameterized as a function of the deformation energy and of ice concentration (Steiner, 2001). With this formulation it is possible to implement drag coefficients in sea ice models without additional parameterizations for ridges and melt ponds formation.

Tsamados et al. (2014) and Steiner (2001) used stand alone sea ice models.

But variations of oceanic drag coefficients also affect the oceanic momentum through the drag coefficients and the drift velocities of the ice that are themselves functions of the atmospheric and oceanic stress. For example, Castellani et al. (2015) showed, based on an idealized experiment, that variations in the Ekman vertical velocity associated with variable oceanic drag coefficients are on the same order of magnitude as the variations due to changes in the surface velocity of the ice. Roy et al. (2015) compare simulations using different air-ice and ocean-ice roughness. They show effects on the general features of sea ice (concentration, thickness, drift) and also on the liquid and solid fresh water budget of the Arctic Ocean. In particular, increased ice-ocean roughness leads to higher Arctic fresh water budget by increasing fresh water retention in the Beaufort Gyre. Martin et al. (2014) investigate changes in momentum transfer to the ocean as consequence of ice thickness and areal extent decrease. They conclude that the weaker ice cover in fall, winter and spring, and the increase in open water fraction in summer cause trends in the momentum transfer over the last three decades. In a more recent work, Martin et al. (2016) analyze the effects that the introduction of variable drag coefficients in numerical models have on the trend of annual mean ocean surface stress. They show that a decrease in surface roughness over the years leads to a decline in surface ocean stress. They conclude that a proper investigation of the trend of the air to ocean momentum transfer in presence of sea ice requires to represent sea-ice surface variations.

In the present study we investigate how atmospheric and oceanic drag coefficients that depend on the degree of sea-ice deformation and on ice concentration affect sea-ice distribution and ocean circulation in a numerical model. We follow the Steiner (2001) deformation energy approach and apply it to a coupled sea ice-ocean model. We focus on the simulated sea-ice properties, but also on effects on and changes in the ocean circulation, with the aim to investigate (1) which of the main physical parameters describing the large scale sea ice cover (ice concentration, thickness and drift) is affected the most, and (2) in which regions of the Arctic these changes are more prominent. Finally, we aim to (3) quantify to what extent the ocean is affected.

In Section 2 we introduce the model configuration and the implemented parameterizations. We also describe the sensitivity study performed to select the set of parameters used in the numerical experiment. The results for sea ice and ocean are presented in Section 3 and then discussed in Section 4. A summary and conclusions follow in Section 5.

2. Methods

2.1. Model Description and Setup

We use the Massachusetts Institute of Technology general circulation model (MITgcm, Marshall et al., 1997) in a coupled ocean–sea-ice Arctic Ocean configuration. The configuration is similar to the NAOSIM configuration of Karcher et al. (2011) and was already described in Castro-Morales et al. (2014). The domain covers the Arctic Ocean, the Nordic Seas, and the North Atlantic down to approximately 50°N (Figure 1). The horizontal resolution of 1/4° corresponds to ∼28 km on a rotated spherical grid with the equator passing though the North Pole. In the vertical, the domain is discretized in 33 levels with thickness ranging from 10 m at the surface to ∼ 350 m at depth. Vertical mixing in the ocean is parameterized by a K-Profile Parameterization (KPP) scheme (Large et al., 1994) and tracers are advected with an unconditionally stable seventh-order monotonicity preserving scheme (Daru & Tenaud, 2004) that requires no explicit diffusivity. The mixed layer depth is diagnosed based on a density criterion (Kara et al., 2000). To apply this criterion, densities are linearly interpolated between model layers to determine the depth at which the density increases above a critical density relative to the surface density. In strong stratification, where density in the second layer is already much higher than in the first layer, this can lead to mixed layer depths smaller than the 10 m of the surface layer thickness. The model variable density is located at the center of the grid cells, so that the topmost density is at 5 m depth. The minimum mixed layer depth is thus 5 m.

The ocean model is coupled with a dynamic-thermodynamic sea-ice model (Losch et al., 2010). The sea-ice model of the MITgcm uses a viscous-plastic rheology and so-called zero-layer thermodynamics (i.e., zero heat capacity formulation, Semtner, 1976) with a prescribed ice thickness distribution (Hibler, 1979, 1980, 1984; Castro-Morales et al., 2014): In order to compute the net heat flux through the ice, the latter is redistributed into seven ice thickness categories between 0 and a maximum thickness of twice the mean thickness. The heat fluxes are computed individually for each thickness and then summed. The shape of the distribution of these seven thicknesses is flat, normalized and fixed in time (see Hibler, 1984; Castro-Morales et al., 2014, their Figure 1). We also use the same parameterization for the snow distribution. In the present configuration the model does not include a dynamic ice thickness distribution (ITD).

The model is forced by realistic atmospheric fields. We use data of the Coordinated Ocean Research Experiment (CORE) version 2 (Large & Yeager, 2009) for the spin-up and the NCEP Climate Forecast System Version 2 (Saha et al., 2014) for the analyzed simulations. A monthly climatology of river runoff for the main Arctic rivers follows the AOMIP protocol (Proshutinsky et al., 2001).

The model is spun up from the first day of January 1948 to the last day of December 1978 in a baseline (control) configuration with constant drag coefficients. The subsequent simulations are forced with NCEP reanalysis data (Saha et al., 2014) from the first day of January 1979 to the last day of December 2010.

2.2. Parameterization of Atmospheric and Oceanic Drag Coefficients

Sea-ice motion is determined mainly by three forces: the internal stresses in the ice, the atmospheric drag force and the oceanic drag force (Steele et al., 1989). The momentum equations for the atmospheric drag $\boldsymbol{\tau}_a$ and the oceanic drag $\boldsymbol{\tau}_w$ are expressed through a quadratic drag relationship:

$$\boldsymbol{\tau}_a = \rho_a c_a |\boldsymbol{U}_a - \boldsymbol{u}| R_a (\boldsymbol{U}_a - \boldsymbol{u}) \,, \tag{1}$$

$$\boldsymbol{\tau}_w = \rho_w c_w |\boldsymbol{U}_w - \boldsymbol{u}| R_w (\boldsymbol{U}_w - \boldsymbol{u}) \,, \tag{2}$$

where ρ_a and ρ_w are the densities of air and sea water. The drag depends on the relative velocities $\boldsymbol{U}_{a,w} - \boldsymbol{u}$ where $\boldsymbol{U}_a$ is the atmospheric wind, $\boldsymbol{U}_w$ is the ocean current and $\boldsymbol{u}$ is the ice drift. The ocean (atmosphere) rotation matrix R_w (R_a) accounts for unresolved Ekman layers. c_a and c_w are the transfer coefficients for momentum, called air drag coefficient and water drag coefficient. From the Monin Obukhov similarity theory and a stability corrected logarithmic profile (Garbrecht et al., 2002) they can be expressed as:

$$c_D = \left[\frac{k}{ln\left(\frac{z_r}{z_0}\right) - \Psi_m\left(\frac{z_r}{L}\right)} \right]^2 \quad , \tag{3}$$

where $D = a$ for the atmosphere and $D = w$ for the ocean, z_r is a reference height (usually 10 m for the atmosphere, or the depth at which the current equals geostrophic flow for the ocean, Lu et al., 2011), z_0 is the roughness length of sea ice, Ψ_m is the Dyer-Businger stability function, L the Monin Obukhov length, and k the von Karman constant. In case of neutral conditions, equation (3) reduces to the expression for the neutral drag coefficients:

$$c_{D,n} = \left[\frac{k}{ln\left(\frac{z_r}{z_0}\right)} \right]^2 \quad . \tag{4}$$

The roughness length z_0 changes regionally and temporally due to the presence and formation of topographic elements over/under the ice. Variability in z_0 implies variability in $c_{D,n}$. The NCEP Climate Forecast System reanalysis that we use here (Saha et al., 2014) already includes the appropriate stability parameterization, thus in this study we focus on the neutral drag coefficients, that is, for the case of neutral stratification of the fluid (water and air). In the following the term drag coefficients always refer to neutral drag coefficients, except when stated otherwise.

In the baseline configuration, the sea ice-ocean model runs with constant atmospheric and oceanic drag coefficients: $c_a = 1 \times 10^{-3}$ and $c_w = 5.4 \times 10^{-3}$,

the latter value corresponds the geostrophic drag coefficient proposed by McPhee (2008). These values are the results of an optimization procedure (Nguyen et al., 2011) and were already used in the present model configuration (Castro-Morales et al., 2014). They correspond to a roughness length z_0 of $\approx 5 \times 10^{-5}$ m for the atmosphere-ice interface and $\approx 22 \times 10^{-3}$ m for the ocean-ice interface.

In order to arrive at drag coefficients that depend on sea-ice topography, we introduce the deformation energy R as a prognostic variable into the sea ice model. The deformation energy represents the sea-ice roughness and evolves in time (Steiner et al., 1999). Deformation energy changes with the work of internal forces in the ice E_{int} and with melting (Martin, 2007):

$$\frac{DR}{Dt} = E_{int} + R \cdot \min(M, 0)\,, \tag{5}$$

where M is the same melting rate that is used to thermodynamically change the ice volume, divided by the ice thickness. By definition, M is negative during melting and positive during freezing. The term E_{int} is derived as the scalar product of the stress tensor $\boldsymbol{\sigma}$ and the strain rate tensor $\dot{\boldsymbol{\varepsilon}}$ (Rothrock, 1975; Martin, 2007):

$$E_{int} = \boldsymbol{\sigma} \cdot \dot{\boldsymbol{\varepsilon}} = \sigma_I \varepsilon_I + \sigma_{II} \varepsilon_{II}, \tag{6}$$

where

$$\begin{aligned} \dot{\varepsilon}_I &= \dot{\varepsilon}_{11} + \dot{\varepsilon}_{22}\ , \\ \dot{\varepsilon}_{II} &= \sqrt{\left(\dot{\varepsilon}_{11} - \dot{\varepsilon}_{22}\right)^2 + 4\dot{\varepsilon}_{12}^2}\ , \end{aligned} \tag{7}$$

and

$$\begin{aligned} \sigma_I &= \tfrac{1}{2}\left(\sigma_{11} + \sigma_{22}\right), \\ \sigma_{II} &= \tfrac{1}{2}\sqrt{\left(\sigma_{11} - \sigma_{22}\right)^2 + 4\sigma_{12}^2} \end{aligned} \tag{8}$$

are invariants of the strain rate tensor $\dot{\boldsymbol{\varepsilon}}$ and of the stress tensor $\boldsymbol{\sigma}$ (Rothrock, 1975). This formulation for the deformation energy was previously implemented in uncoupled sea-ice models (Steiner et al., 1999; Martin, 2006, 2007).

Many studies focusing on the dependency of neutral drag coefficients on surface roughness (e.g. Garbrecht et al., 1999, 2002; Lüpkes et al., 2012, 2013; Lüpkes & Gryanik, 2015) are based on the the partitioning approach by Arya (1973, 1975). According to this approach, the neutral drag coefficient is given as the sum of a skin drag, accounting for small-scale roughness, and a form drag, accounting for the influence of large obstacles (due to a pressure difference before and behind the obstacle). This can be written as:

$$c_D = c_D^{\text{skin}} + c_D^{\text{form}} \quad . \tag{9}$$

The form drag is usually expressed based on geometric consideration of the obstacles such as ridges (Garbrecht et al., 1999, 2002), melt ponds and ice floes (Lüpkes et al., 2012, 2013; Lüpkes & Gryanik, 2015). Following Steiner (2001), the drag coefficients are expressed as a function of deformation energy R and ice concentration A:

$$c_a\left(R, A\right) = b_a + m_a R + d_a \left[1 - 4\left(A - \frac{1}{2}\right)^2\right] , \tag{10}$$

$$c_w\left(R, A\right) = b_w + m_w R + d_w \left[1 - 4\left(A - \frac{1}{2}\right)^2\right] . \tag{11}$$

The skin drag (the terms b_a and b_w in equations (10) and (11)) accounts for small scale roughness and it is chosen following Steiner (2001) according to the lowest observed drag coefficients: $b_a = 0.8 \times 10^{-3}$ and $b_w = 1.2 \times 10^{-3}$ (see e.g., Shirasawa & Aota, 1991; Shirasawa & Ingram, 1991; Wamser & Martinson, 1993). The form drag accounts for large scale obstacles and it is parameterized as a function of deformation energy R (second term on the right hand side of equations (10) and (11)) and of ice concentration (third term on the right hand side of equations (10) and (11)). According to equations (10) and (11), the drag coefficients increase linearly with the deformation energy and depend quadratically on ice concentration with a maximum of d_a (d_w) at $A = 0.5$ (50% ice concentration, see also Figure 1 in Steiner, 2001). Initially, the values of the parameters m_a, m_w, d_a and d_w are set to the values optimized via comparison

with observed buoy-drift velocities (Steiner, 2001, see also Table 2). In Section 2.3, they are optimized by performing a quantitative comparison with sea-ice observations.

Note, that in this configuration the deformation energy does not affect the sea ice or the ocean directly because the sea-ice model does not employ a dynamic ice thickness distribution (ITD, as in, e.g., Ungermann et al., 2017). This means that we do not redistribute the ice between thickness categories according to variations of deformation energy. The only feedback on the physics of the model is through the atmospheric and oceanic drag coefficients that enter the momentum equations of the sea ice and of the ocean. Even without an ITD, which may increase the general realism of the simulation (Ungermann et al., 2017), the main feedback we would expect in the context of the drag coefficients is present in our model. The shape of the ITD is not enough to distinguish between an ensemble of flat, thermodynamically grown floes with different thicknesses (and comparably low drag coefficients) or an ice pack with a high coverage of melt ponds, pressure ridges and floe edges (and comparably high drag coefficients). For this reason, even very detailed parameterizations of variable drag coefficients have only indirect connections between the ITD and the drag coefficients via intermediate variables (Tsamados et al., 2014). But the main feedback we would expect in this context is included in the model: When ice ridges, its thickness increases (which should make it harder to deform) yet at the same time the pressure ridges lead to a higher drag coefficient, that should increase the deformation of already thick ice.

2.3. Choice of parameters

Equations (10) and (11) contain 6 parameters: b_a, b_w, m_a, m_w, d_a and d_w. The skin drags b_a and b_w are directly constrained by observations (e.g., Shirasawa & Aota, 1991; Shirasawa & Ingram, 1991; Wamser & Martinson, 1993). In order to find the best set of parameter values for m_a, m_w, d_a and d_w, we compare the model results with observations in a sensitivity study. To evaluate our model results quantitatively we use a cost function from satellite

observations as a measure for model quality (Ungermann et al., 2017). In a second step, we use a Green's functions approach to obtain a set of optimal parameters (for details see Menemenlis et al., 2005; Ungermann et al., 2017). The cost function for a given variable (concentration, thickness, drift) in a given time frame (month/season) is defined as:

$$F_{\mathrm{var}} = \sum_{i=1}^{N_{\mathrm{var}}} \frac{1}{2} \frac{(x_i - y_i)^2}{N_{\mathrm{var}} \xi_i^2} \tag{12}$$

where y_i is a single observation, x_i the model estimate at the same position and time, and ξ_i the measurement uncertainty of this observation. N_{var} is the number of observations of the respective variable, so that the contribution of each variable is normalized. In Table 3 we present the cost function for the different data sets and seasons, that is the sum over the amount of data available for a specific variable in a certain time frame. The total cost function is the sum of all contributions.

Most, if not all, data assimilation and optimization methods (e.g., Massonnet et al., 2014; Roach et al., 2018) are based on minimizing a cost function similar to ours. The methods differ in the way the errors are treated and how the minimum of the cost function is found. For example, an Ensemble Kalman Filter allows to estimate the error covariances of the state during the optimization procedure and use this information to refine the results (e.g., Massonnet et al., 2014). The cost function can be linearized and an optimal set of parameters can be found with approximated gradient information, for example with a Gauss-Newton method (Roach et al., 2018). In our approach, all prior covariance information about the unknown parameters is neglected and the cost function is constructed with a diagonal error covariance matrix from the error estimates of the observations. This allows us to use the Green's Function approach and to explicitly calculate an optimal set of parameters in each step without an additional line search that would be necessary in the (more generally applicable) Gauss-Newton method.

We use four different datasets: 1) the reprocessed concentration dataset from OSISAF (EUMETSAT, Ocean and Sea Ice Satellite Application Facility, 2011)

and its error estimates (1979 - 2009); (2) the ICESat-JPL thickness product (Kwok & Cunningham, 2008) with a local error estimated as in Kauker et al. (2015) yet with an upper limit of 1 m for the uncertainty (March as well as October/November, 2003 - 2008); (3) the OSISAF winter sea ice drift (Lavergne et al., 2010, October to April, 2002 - 2006) and (4) the summer sea-ice drift from Kimura et al. (2013) (May to July, 2003 - 2007), which both use passive-microwave satellite data, with error estimates of Sumata et al. (2014, 2015). For ice concentration we compute the cost function separately for winter and for summer, and for ice thickness separately for March and November.

The choice of model parameters follows Nguyen et al. (2011), their Table 2. They include albedo (dry ice, wet ice, dry snow, wet snow), air-ice drag and similar with the other drags, ice strength, lead closing, vertical diffusivity, salt plume, and a river runoff factor. This set of parameters with a model configuration identical to ours was shown to yield simulations consistent with observations (see Castro-Morales et al., 2014, their Figure 7). Since our main interest is in the drag coefficients, we focus our sensitivity study only on the parameters m_a, m_w, d_a and d_w in equations (10) and (11). In Table 2 we list the values of the original parameters and the final values after two optimization cycles. In this study we compare three different model runs: DRAGS, using the optimized parameters to compute variable drag coefficients; MEAN, using constant drag coefficients (to keep the Nansen number $\mathrm{Na} = \sqrt{\rho_a c_a / \rho_w c_w}$ comparable we use the mean values from DRAGS as constant drag coefficients, see Table 4); and CTRL using constant drag coefficients with the original values (Castro-Morales et al., 2014). The cost function values of these configurations are given in Table 3. While our main results are obtained from a model-to-model comparison, we show a qualitative comparison with observations of ice concentration and ice thickness for the DRAGS run as results of the optimization procedure (Figure 2) to demonstrate the realism of our coupled ice-ocean model. The most remarkable model biases are an overestimation of the ice edge in the Fram Strait, especially in Winter, and a dipole pattern in the thickness field (March RMSE = 0.69, November RMSE = 0.59), with a thick bias in the

Barents Sea and the East Siberian Sea, and a thin bias over the central Arctic, both a common problem of many models of comparable complexity (Stroeve et al., 2014). These model-data comparisons place the realism of our model configuration well in the range of CMIP5 sea ice components.

3. Results

In this section we present results for climatologies obtained from the first day of January 1990 to the last day of December 2010. The first ten years (1979-1989) of the simulations are not used because during this time the model adapts to the new forcing and to the new physics. We focus our analysis on the months of March (maximum sea-ice extent) and September (minimum sea-ice extent).

The model domain with the following regions is shown in Figure 1: Lincoln Sea (LS), Central Arctic (AC), Beaufort Sea (BS), East Siberian Sea (ESS), and Laptev Sea (LapS).

3.1. Simulated Deformation Energy and Drag Coefficients

Values for deformation energy in the Arctic basin vary between 20 and $300\,\mathrm{kJ/m^2}$ (Figure 3). Lower values are found towards the Marginal sea Ice Zone (MIZ) whereas values higher than $300\,\mathrm{kJ/m^2}$ characterize the coastal areas along the north coast of Greenland and the north coasts of the Arctic Canadian Archipelago, where ice is usually pushed against land and thus more deformed. In the Central Arctic the values vary between 25 and $95\,\mathrm{kJ/m^2}$, in agreement with Steiner et al. (1999).

The distribution of drag coefficient values is governed by the linear dependence on the deformation energy (equations (10) and (11)). The impact of ice concentration is only visible where $A<1$ (not shown). Simulated atmospheric and oceanic drag coefficients are higher in summer than in winter (Table 5). Maximum values of both atmospheric and oceanic drag coefficients are found in the Lincoln Sea, minimum values in the Laptev Sea. Oceanic drag coefficients

show a larger variability (due to larger values of m_w and d_w compared to m_a and d_a in equations (10) and (11)) in both summer and winter.

Changes in drag coefficients reflect changes in the roughness length z_0 (Section 2.2). In order to calculate the roughness length for the atmosphere, that is for the upper sea-ice surface, and for the ocean, that is for the surface underneath the ice, we use equation (4) with 10 m as reference height for the atmosphere and 5 m for the ocean as in Shaw et al. (2008). Values of surface roughness length vary between 0.7×10^{-5} m and 0.027 m (Figure 4a-b). These results compare well with the values of roughness length for different ice classes in Guest & Davidson (1991). In particular, the maximum value of 0.027 m is the same as the value of 0.027 m for very rough ice in Guest & Davidson (1991). The mean value in the Lincoln Sea (Table 6) agrees with the value of 2.0×10^{-3} for smooth MYI, whereas the mean values in BS, CA, ESS and LapS (Table 6) agree with the values for very smooth and smooth FYI (Guest & Davidson, 1991). Values for the under-ice roughness length varying from 0.05×10^{-3} m to 0.16 m (Figure 4c-d) are also in agreement with observations (Shaw et al., 2008; Johannessen, 1970; Shirasawa, 1986; Shirasawa & Ingram, 1991).

3.2. Contributions to atmospheric and oceanic drag coefficients

To analyze the causes of the regional and seasonal differences in atmospheric and oceanic drag coefficients, we look at the contribution in equations (10) and (11) of the terms due to deformation energy and ice concentration as ratios between skin drag, deformation energy term and ice concentration term over the total atmospheric drag coefficients (Figure 5), and oceanic drag coefficients (not shown). In winter, the skin drag dominates both atmospheric and oceanic drag coefficients, mainly in the Eastern sector of the Arctic Ocean. In summer, the skin drag dominates in the MIZ, where the deformation energy is low and the ice concentration is lower than 0.5. The deformation energy term dominates in the Western sector of the Arctic Ocean and its contribution is generally higher in winter. The contribution of the ice concentration term in winter is negligible almost everywhere in the Arctic Basin, except for the MIZ, which in

winter extends to the Barent Sea and south of the Svalbard Islands. In summer, its contribution increases everywhere in the Arctic Ocean with maxima in the Laptev Sea of up to 80% of the total drag coefficient values.

To analyze in more detail the contribution of deformation and ice concentration in the computation of the atmospheric drag coefficients, we show in Figure 6 the time evolution (from 1990 to 2010) of mean atmospheric drag coefficients due to deformation energy and due to ice concentration in some regions of interest. In general, the contribution due to ice concentration shows a larger seasonal variability since in winter the ice concentration approaches 1 almost everywhere in the Arctic and the ice concentration term drops to zero. The contribution of the two terms is different for different regions, and shows also an interannual variability. In the Lincoln Sea, the total atmospheric drag is always dominated by deformation. In the Central Arctic, the deformation energy term dominates in winter, whereas in summer the drag is dominated by the ice concentration term. In the Laptev Sea (not shown) the contribution of the deformation energy remains always very small. In the Beaufort Sea the contribution of the two terms varies with time, the same holds for the East Siberian Sea (not shown).

3.3. Sea Ice

Mean summer ice concentration is lowest in the Laptev Sea and East Siberian Sea ($A < 0.4$) and highest in the Lincoln Sea and the Central Arctic ($A > 0.8$) in both DRAGS and MEAN (Table 7). In winter, the differences between the two runs (DRAGS-MEAN) in ice concentration are visible only in the MIZ (Figure 7a). In summer, the ice concentration is reduced almost everywhere in the Arctic basin when we introduce variable drag coefficients (DRAGS), except for the Beaufort Sea (Figure 7b). In both winter and summer the differences remain between 10% and 20%.

Mean summer ice thickness in the Arctic Ocean ranges from 0.5 m in the East Siberian Sea and Laptev Sea to up to 7 m in the Lincoln Sea (Table 7). Between DRAGS and MEAN the ice thickness differences in the western sector of the Arctic Ocean are on the order of 0.5 m in both March and September. In

the Lincoln Sea differences are larger than 1 m.

In our simulations, summer sea ice velocities are on the order of 5 cm s^{-1} in the Arctic Ocean. Faster ice is a characteristic of the Beaufort Sea (with 5.25 cm s^{-1} in DRAGS and 4.90 cm s^{-1} in MEAN). Very low values are found in the Lincoln Sea where the ice remains constrained between the coasts of Greenland and Ellesmere Island and it is characterized by velocities smaller than 1 cm s^{-1}. North of Greenland and in the Fram Strait the ice moves faster in DRAGS than in MEAN and the arrows indicate a larger export of ice through the Fram Strait. In summer, when the ice is more mobile, differences are larger and the pattern of these differences is more pronounced. The drift difference arrows show the anticyclonic pattern in the Beaufort Gyre (Figure 7f) that usually dominates in summer, thus showing an increased anticyclonic circulation in DRAGS than in MEAN.

3.4. Ocean Surface

In order to evaluate the effects of the new drag formulation on the surface ocean, we analyze sea surface temperature θ, surface salinity and Mixed Layer Depth (MLD).

In winter, temperatures are equal to the freezing point everywhere in the Arctic Ocean, except in the MIZ (Figure 8 and Table 7). In summer (Figure 8b) the coldest temperatures are found in the Nansen Basin. Mean values vary between $-0.24\,^{\circ}$C in the East-Siberian Sea and $-1.66\,^{\circ}$C in the Lincoln Sea. Temperature differences between DRAGS and MEANS are no larger than $0.06\,^{\circ}$C.

Surface salinity in winter ranges between 33 and 35 except for the Beaufort Sea and East-Siberian Sea, where values are lower than 32 (Figure 9a). The surface salinity differences in winter are on the order of 0.2 except for the Laptev Sea and Kara Sea with differences up to 0.5.

On average, the mean MLD in September is deeper by 3 m in the DRAGS run than in the MEAN run (Fig 10a, c). This is a big difference because in the MEAN run the MLD reaches average summer depths in the sea ice covered

area of 8 m±2 m. In winter, the mixed layer is deeper everywhere in the Arctic Basin for both MEAN (39±11m) and DRAGS (43±12 m). The MLD differences DRAGS - MEAN are smaller in winter than in summer. Note that the model layer thickness is 10 m at the surface and we use a density criterion (Section 2) to estimate MLDs. The impact of variable drag coefficients on the MLD should be tested using an ocean model that can resolve the ocean surface at a finer scale (1-3 m). In this case, though, the approach used in the present work, i.e. using the computed drag coefficients to calculate the ocean currents in the first surface layer, would result erroneous (Roy et al., 2015).

3.5. Ocean Interior

We evaluate the effects of the new drag parameterization on the ocean interior by analyzing the September stream function, which specifies the character (cyclonic or anticyclonic) of the flow, a vertical salinity profile along an oceanic transect through a large freshwater reservoir in the Beaufort Sea in September (Figure 1), and the circulation in the mid Atlantic Water (mid-AW) layer between 350 m and 800 m depth.

The stream function (Figure 10) is computed by vertically integrating the climatological horizontal velocity for September. It illustrates the well-known Arctic circulation pattern with a more or less clear separation between the Eurasian and Canadian Basin (Steiner et al., 2004). There is a strong anticyclonic circulation in the Beaufort Sea that reflects the surface Beaufort Gyre, whereas the Central Arctic ocean circulation is dominated by a cyclonic pattern of the Atlantic water in the ocean interior. The differences DRAGS - MEAN (Figure 10d) point to a stronger Beaufort Gyre in DRAGS in agreement with the ice drift: stronger ice drift leads to an intensified anticyclonic circulation also in the upper ocean layer. The cyclonic pattern in the central Arctic Ocean interior is also stronger.

The vertical salinity profile (Figure 11a) down to 250 m for the DRAGS run shows the accumulation of fresher water at the surface of the Beaufort Sea. The 32 isohaline reaches down to ca. 150 m. The difference map DRAGS - MEAN

(Figure 11b) shows a thin layer of saltier water at the surface (first 10 meters) in agreement with Figure 9d. In the deep Beaufort sea, the difference map shows fresher water extending to $\sim$120 m depth. In the Central Arctic (CA) the DRAGS run water masses are saltier, with differences extending down to $\sim$250 m depth.

Finally, we compare the circulation of the Atlantic water in the mid-AW layer. In Figure 12a we show the mid-AW circulation in the DRAGS run. The typical pattern as inferred from observations (Carmack et al., 1995; Rudels et al., 1994, 1999; Swift et al., 1997) and previous model results (Holland et al., 1996; Karcher & Oberhuber, 2002; Karcher et al., 2003) is represented. The circulation is cyclonic in the Beaufort Sea-Canadian Basin and in the Makarov Basin. The inflow from the Fram Strait with a branch of mid-AW flowing along the continental margins of the Eurasian and Makarov Basin is also represented. Finally, the mid-AW flows along the continental slope of Greenland and leaves through the Fram Strait. The cyclonic circulation in the Beaufort Sea is slightly slower in the DRAGS run (Figure 12b). A stronger flow of mid-AW between the Alpha Ridge and Makarov Basin is directed towards the Fram Strait. Also the flow along the Lincoln Shelf is enhanced. In the Makarov Basin the cyclonic mid-AW circulation is slowed down for DRAGS compared to MEAN.

3.6. Differences between new mean drag coefficients and original values

The newly implemented drag coefficients parameterization not only leads to more variability, but also to mean drag coefficients that are generally larger (atmosphere) or smaller (ocean) than the default values of CTRL. This implies a change in the Nansen number between MEAN and CTRL that can lead to changes in sea-ice drift and sea-ice properties. In particular, we expect faster ice as a result of the higher atmospheric drag coefficients (1.36×10^{-3} compared to 1×10^{-3}) and the lower oceanic ones (2.82×10^{-3} compared to 5.4×10^{-3}). This motivates an additional comparison for the simulated sea-ice properties between the MEAN run and the CTRL run. Mean values of sea-ice concentration, thickness and drift for the entire Arctic Basin and for regions of interested

are listed in Table 7. Difference maps for sea-ice concentration, thickness and drift in March and September are shown in Figure 13.

Differences in ice concentration are larger in September than in March. During winter, the ice concentration is 1 almost everywhere in the Arctic Ocean, so differences are seen only in the MIZ (Figure 13a). In summer, the sea-ice areal extent in MEAN is reduced in the Central Arctic Basin, Lincoln Sea and Beaufort Sea (Table 7). A stronger reduction is seen in the East Siberian Sea, Laptev Sea and Kara Sea. Ice thickness (Figure 13c and d) is reduced in large parts of the Arctic Basin in winter, with the exception of the Chukchi Sea where the ice thickness in MEAN is ~ 0.5 m larger than in CTRL. In summer, the pattern is the same, with a general reduction of ice over the entire Arctic Ocean. Large differences are seen in the Lincoln Sea with mean summer ice thickness decreasing from 8.46 m in CTRL to 7.86 m in MEAN. The ice moves faster in MEAN than in CTRL, as expected by the change in the Nansen number. Particularly, the circulation patterns are enhanced in both winter and summer. Figures 13e and f show a stronger Beaufort Gyre, and a stronger transpolar drift stream. Differences are relevant in the Lincoln Sea with changes in mean summer drift from $0.02\,\mathrm{cm\,s^{-1}}$ in CTRL to $0.11\,\mathrm{cm\,s^{-1}}$ in MEAN, and in the Central Arctic with an increase from $1.58\,\mathrm{cm\,s^{-1}}$ in CTRL to $2.43\,\mathrm{cm\,s^{-1}}$ in MEAN.

4. Discussion

With the implementation of equations (10) and (11), drag coefficients vary according to season and region (not shown): Between 0.88 $\times 10^{-3}$ and 4.68 $\times 10^{-3}$ for atmospheric drag coefficients, and between 1.28 $\times 10^{-3}$ and 13.68 $\times 10^{-3}$ for the oceanic ones. Our computed atmospheric and oceanic drag coefficients fall into the range of observed and topography-based estimated values (see Table 1), but never reach the extremes. The Steiner (2001) approach relies on the fraction of energy that goes into deformation and is thus responsible for an increase in surface roughness and in drag coefficients. This contribution is expressed by the terms m_a and m_w in equations (10) and (11). These terms

cannot be measured directly in the field and thus represent a large uncertainty of the parameterization.

Our results for different regions represent the general pattern shown in large scale estimates based on satellite data (Petty et al., 2017) with higher values in regions where the ice is more deformed due to proximity to the coast (Lincoln Sea) and due to convergent drift (Central Arctic), and lower values in the marginal seas (Laptev Sea and East Siberian Sea).

Atmospheric drag coefficients computed in a different sea ice model (Tsamados et al., 2014) and based on different parameterizations (Lüpkes et al., 2013) than ours, vary between 0.3×10^{-3} and 4×10^{-3}, whereas oceanic drag coefficients vary between 2×10^{-3} and 20×10^{-3}, in good agreement with our results. The extra contribution of melt pond edges on the atmospheric drag coefficients (not included explicitly in our parameterization) is visible in summer, particularly in July and August (see Tsamados et al., 2014, their Figure 7). In these months, however, the contribution of melt pond edges to the total drag coefficients is much smaller than the other terms (deformation, ice concentration, skin drag). The form drag contribution to the total drag in Tsamados et al. (2014) is based on an ITD model, where the amount of thick, ridged ice in a grid cell is used to estimate geometric parameters (i.e. sail height and distance between sails, and keel depth and distance) to be used in the parameterization for drag coefficients. In contrast, we rely on the deformation energy as an explicit function of internal forces in the ice and from which we derive the drag coefficients. In spite of these differences, our results are very similar to those of Tsamados et al. (2014) in many respects: drag coefficients are higher in summer than in winter, and the contribution of the different terms differ with season, that is, in winter the total drag is dominated by deformation, whereas in summer the drag is dominated by the ice concentration term.

The newly implemented parameterization affects the simulated sea-ice properties, that is, extent, thickness and drift. In general, the ice moves faster, is thinner, and the overall area is reduced (Table 7). In particular, the sea-ice drift increase in the western part of the Arctic results in a decrease of ice thickness,

particularly in the Lincoln Sea and along the north coast of Greenland, region where the highest atmospheric drag coefficients are found. The larger sea-ice velocities along the north coast of Greenland directed towards the Fram Strait explain the reduction of ice concentration in the same region. Correlations between differences in ice thickness and ice velocities are significant but weak ($|r| < 0.2$) for the entire Arctic Basin and for most of the regions of interest. Exceptions are the Lincoln Sea, with r = -0.28 between changes in ice thickness and changes in sea ice drift, and the Central Arctic with r = -0.29.

To compare the realism of the different simulations, we use a cost function computed for the different sea ice variables in winter and in summer (Table 3). The total cost function value, that is, the model-data misfit is smaller for the DRAGS run than for the MEAN run. In particular, the ice concentration in both summer and winter, the March ice thickness and the summer sea-ice drift are better simulated with the variable drag coefficients. The default values of constant drag coefficients in the CTRL run gives the largest model-data misfit (largest cost function), except for winter ice concentration. The differences DRAGS - CTRL in winter ice concentration (not shown) point to a southward shift of the marginal ice zone. This is due to the larger Nansen number in DRAGS that makes the ice more mobile.

In general, the differences between MEAN and CTRL are larger than between DRAGS and MEAN. We conclude that the variable drag parameterization improves the model simulation, but to first order, this improvement can already be achieved by adjusting the mean drag coefficients and hence the Nansen number. We can thus suggest a new set of constant drag coefficients that improve the simulated sea-ice characteristics. Additional improvement in the model simulations is caused by the spatial variability of the drag coefficients.

With variable drag coefficients in the DRAGS run mixing tends to be stronger leading to deeper mixed layers. MLDs estimates from observations are sparse. In summer, the few available ones range from 8 m to 20 m in the Beaufort Sea (Yang et al., 2004; Lemke & Manley, 1984; Peralta-Ferriz & Woodgate, 2015). The mean MLD of 10 m in the DRAGS run agrees better with these estimates

than the 7 m in the MEAN run. MLD data based on the NOAA World Ocean Atlas (Monterey & deWitt, 1997) give a mean value of 8.7 m (and values up to 440 m) for the entire Arctic Basin in September. Here, the mean MLD of 8±2 m in the MEAN run appears to be closer to observation than the mean of 11±2 m in the DRAGS run, but this is confounded by the large range of MLDs in the observations and the ambiguous estimation methods. In winter in the Central Arctic, MLD values are between 25 m and 50 m (Treshnikov & Baranov, 1973), compared to the simulated 42 m in both MEAN and DRAGS. In general, the agreement with independent estimates of MLDs is ambiguous and both DRAGS and MEAN agree with observational estimates similarly well. We remind that our numerical surface ocean layer is 10 m thick and MLDs are sometimes smaller making our MLD estimates less accurate than with a model with higher vertical resolution.

Changes due to variable drag coefficients in sea surface temperatures are small in most regions. Note that in the present model study the heat exchange coefficients do not depend on the surface roughness, thus the changes in surface temperature are only an indirect consequence of the changes in the sea-ice properties. The pattern in surface temperature changes does not suggest any trend. In the Lincoln Sea the reduction in ice thickness correlates with an increase in temperature (r = -0.39), pointing to an increased heat flux that penetrates the thinner ice and reaches the ocean surface. A similar strong correlation is found in the Central Arctic (r = -0.5), whereas in the other regions the correlation is significant but weak.

Differences in salinity point to a more saline sea surface in summer and fresher water in the interior of the Beaufort Sea. The amount of fresh water relative to a reference salinity of 34.8 (Proshutinsky et al., 2009; Roy et al., 2015) in the Beaufort Sea (not shown here) is larger in DRAGS than in MEAN. This agrees with Roy et al. (2015) who show an increased fresh water retention in the Beaufort Gyre due to stronger ice-ocean and air-ice roughness. The mean values of atmospheric and oceanic drag coefficients in the Beaufort Sea (see Table 5) point to a larger surface and bottom-surface roughness in this region compared

to the values in MEAN. Moreover, Figure 7f shows a stronger Beaufort Gyre, which explains the retention of fresh water in that region. The total liquid Arctic fresh water budget is higher in MEAN than in the DRAGS and in the CTRL runs, but the differences remain very small.

5. Summary and Conclusion

Atmospheric and oceanic drag coefficients vary in time and space as a consequence of the interplay between sea-ice deformation and sea-ice concentration. In the present study, we introduce variable atmospheric and oceanic drag coefficients in a coupled sea-ice–ocean model and we quantify the effects of the new parameterization on the main sea-ice properties and on the ocean. This is achieved by comparing three simulations: two simulations with constant drag coefficients and a simulation where the drag coefficients are parameterized as a function of ice concentration and deformation energy.

Simulated atmospheric and oceanic drag coefficients fall in the range of observed values and agree with recent estimates based on topography profiles and model results. In our study resulting atmospheric and oceanic drag coefficients can evolve spatially and temporally as function of sea-ice characteristics: In winter, drag coefficients are dominated by sea-ice deformation, whereas in summer ice concentration contributes most.

The dynamic sea-ice state is affected by the new parameterization. Particularly in summer, the ice moves faster, is thinner, and the areal extent is reduced when variable drag coefficients are used. The ice thickness shows differences up to 0.5 m in the Arctic basin. In the Lincoln Sea more ice is removed due to higher drag coefficients and thickness differences are up to 1 m, pointing to a strong reduction of ice volume in that region. The variable drag parameterization does not have a uniform effect in the Arctic basin, but the impact is more visible in the western sector of the Arctic. With variable drag coefficients the model misfit with observations is improved, particularly for sea-ice thickness in March, sea-ice drift in summer, and sea-ice concentration in summer and winter.

The mean values of drag coefficients computed from the run with variable ones are a better set of parameters for simulations with constant drag coefficients. The new set of constant drag coefficients is obtained by the optimization of a sophisticated drag coefficient parameterization and differ from values emerging by a different optimization.

Our study represents the first implementation of a parameterization for surface dependent drag coefficients in a coupled sea ice-ocean model. Not only does this approach allow a more physical representation of the sea-ice evolution by including the sea-ice–ocean feedbacks, but also it makes possible the analysis of its effects on the ocean circulation. With the new implementation, surface mixing is stronger, and causes a deeper mixed layer, particularly in summer. Finally the effects of the newly implemented parameterization reach the ocean interior causing changes in Atlantic water circulation. Based on the analysis of climatological maps these effects are small.

The model configuration used in the present study allows us to investigate the main feedbacks due to variable drag coefficients. Nevertheless, this configuration is simple and the effects of variable drag coefficients should be tested on a more complex model including an ITD and an ice strength parameterization. Moreover, the effects on the mixed layer depth should be tested using a model with a better vertical resolution in the surface ocean.

In a natural continuation of this study, the effects of our parameterization implementation on the atmosphere and ensuing feedbacks should be studied in a coupled atmosphere-ice-ocean model. Finally, in the light of the recent increase in sea-ice drift (Spreen et al., 2011; Kwok et al., 2013), our results may be even more relevant to the community.

Acknowledgments

We thank the CLIVAR (Climate and Ocean Variability, Predictability, and Change) working group for the release of CORE version 2, the NOAA's National Centers for Environmental Prediction (NCEP) for developing the NCEP-CFSv2

data set, and the Arctic Ocean Model Intercomparison Project (AOMIP, now FAMOS - Forum for Arctic Modeling & Observational Synthesis) for the release of the river runoff climatology. We would like to thank Michael Karcher, Frank Kauker, Hiroshi Sumata, and Kathrin Riemann-Campe, all affiliated with the Alfred Wegener Institute (AWI), for the interesting discussions that helped to understand and interpret the results.

References

Andreas, E. L., Horst, T. W., Grachev, A. A., Persson, P. O. G., Fairall, C. W., Guest, P. S., & Jordan, R. E. (2010). Parametrizing turbulent exchange over summer sea ice and the marginal ice zone. *Q. J. R. Meteorol. Soc.*, *136(694)*, 927–943.

Arya, S. P. S. (1973). Contribution of form drag on pressure ridges to the air stress on Arctic ice. *J. Geophys. Res.*, *78(30)*, 7092–7099.

Arya, S. P. S. (1975). A drag partitioning theory for determining the large-scale roughness parameter and wind stress on the Arctic pack ice. *J. Geophys. Res.*, *80(24)*, 3447–3454.

Birnbaum, G., & Luepkes, C. (2002). A new parameterization of surface drag in the marginal sea ice zone. *Tellus*, *A, 54*, 107–123, doi: 10.1034/j.1600–0870.2002.00243.x.

Carmack, E. C., Macdonald, R. W., Perkin, R. G., McLaughlin, F. A., & Pearson, R. J. (1995). Evidence for warming of Atlantic water in the Southern Canadian Basin of the Arctic Ocean: Results from the Larsen-93 Expedition. *Geophys. Res. Lett.*, *22(9)*, 1061–1064, doi: 10.1029/95GL00808.

Castellani, G., Gerdes, R., Losch, M., & Lüpkes, C. (2015). Impact of Sea-Ice Bottom Topography on the Ekman Pumping. In G. Lohmann, H. Meggers, V. Unnithan, D. Wolf-Gladrow, J. Notholt, & A. Bracher (Eds.), *Towards an Interdisciplinary Approach in Earth System Science* Springer Earth System

Sciences (pp. 139–148). Springer International Publishing. doi:10.1007/978-3-319-13865-7_16.

Castellani, G., Lüpkes, C., Hendricks, S., & Gerdes, R. (2014). Variability of Arctic sea ice topography and its impact on the atmospheric surface drag. *J. Geophys. Res. Oceans*, *119*, 6743–6762, doi:10.1002/2013JC009712.

Castro-Morales, K., Kauker, F., Losch, M., Hendricks, S., Riemann-Campe, K., & Gerdes, R. (2014). Sensitivity of simulated Arctic sea ice to realistic ice thickness distributions and snow parameterizations. *J. Geophys. Res. Oceans*, *119*, 559–571, doi:10.1002/2013JC009342.

Curry, J. A., Schramm, J. L., & Ebert, E. E. (1995). Sea Ice-Albedo Climate Feedback Mechanism. *Journal of Climate*, *8*, 240–247.

Daru, V., & Tenaud, C. (2004). High order one-step monotonicity-preserving schemes for unsteady compressible flow calculations. *J. Comp. Phys.*, *193(2)*, 563–594, doi: 10.1016/j.jcp.2003.08.023.

EUMETSAT (Ocean and Sea Ice Satellite Application Facility, 2011). Ocean and Sea Ice Satellite Application Facility (2011), Global sea ice concentration reprocessing dataset 1978-2009 (v1.1). URL: `http://osisaf.met.no`.

Flocco, D., & Felthman, D. L. (2007). A continuum model of melt pond evolution on Arctic sea ice. *J. Geophys. Res. Oceans*, *112(C08016)*, doi:10.1029/2006JC003836.

Flocco, D., Felthman, D. L., & Turner, A. K. (2010). Incorporation of a physically based melt pond scheme into the sea ice component of a climate model. *J. Geophys. Res. Oceans*, *115(C08012)*, doi:10.1029/2009JC005568.

Garbrecht, T., Luepkes, C., Augstein, E., & Wamser, C. (1999). Influence of a sea ice ridge on low-level airflow. *J. Geophys. Res.*, *104*, 24,499–24,507.

Garbrecht, T., Lüpkes, C., Hartmann, J., & Wolff, M. (2002). Atmospheric drag coefficients over sea ice - validation of a parameterisation concept. *Tellus*, *A, 54*, 205–219, doi: 10.1034/j.1600–0870.2002.01253.x.

Guest, P., & Davidson, K. L. (1991). The aerodynamic roughness of different types of sea ice. *J. Geophys. Res. Oceans*, *96(C3)*, 4709–4721, doi:10.1029/90JC02261.

Haas, C., Pfaffling, A., Hendricks, S., Rabenstein, L., Etienne, J.-L., & Rigor, I. (2008). Reduced ice thickness in Arctic Transpolar Drift favors rapid ice retreat. *Geophys. Res. Lett.*, *35(L17501)*, doi:10.1029/2008GL034457.

Hibler, W. D. (1979). A dynamic thermodynamic sea ice model. *J. Phys. Oceanogr.*, *9*, 815–846.

Hibler, W. D. (1980). Modeling a variable thickness sea ice cover. *Mon. Weather Rev.*, *108*, 1943–1973.

Hibler, W. D. (1984). The role of sea ice dynamics in modeling CO_2 increases. In J. E. Hansen, & T. Takahashi (Eds.), *Climate Processes and Climate sensitivity*. AGU, Washington, D. C., doi: 10.1029/GM029p0238.

Holland, D. M., Mysak, L. A., & Oberhuber, J. M. (1996). An investigation of the general circulation of the Arctic Ocean using an isopycnal model. *Tellus*, *A, 48*, 138–157. doi: 10.1034/j.1600–0870.1996.00008.x.

Hunke, E. (2010). Thickness sensitivities in the CICE sea ice model. *Ocean Mod.*, *34*, 137–149, doi:10.1016/j.ocemod.2010.05.004.

Hunke, E. C., Lipscomb, W. H., & Turner, A. K. (2010). Sea-ice model for climate study: retrospective and new directions. *J. Glaciol.*, *56*, 1162–1172.

Hunke, E. C., Lipscomb, W. H., Turner, A. K., Jeffery, N., & Elliott, S. (2015). CICE: the Los Alamos Sea Ice Model Documentation and Software User's Manual. Version 5.1, LA-CC-06-012, . *Los Alamos Natl. Lab., Los Alamos, N. M.*.

Johannessen, O. M. (1970). Note on some vertical profiles below ice floes in the Gulf of St. Lawrence and near the North Pole. *Journal of Geophysical Research*, *75*, 2857–2861. doi:10.1029/JC075i015p02857.

Kara, A. B., Rochford, P. A., & Hurlburt, H. E. (2000). An optimal definition for ocean mixed layer depth. *Journal of Geophysical Research: Oceans*, *105*, 16803–16821. doi:10.1029/2000JC900072.

Karcher, M., Beszcynska-Moeller, A., Kauker, F., Gerdes, R., Heyden, S., Rudels, B., & Schauer, U. (2011). Arctic Ocean warming and its consequences for the Denmark Strait overflow. *J. Geophys. Res.*, *116(C02037)*, doi:10.1029/2010JC006265.

Karcher, M., Gerdes, R., Kauker, F., & Köberle, C. (2003). Arctic warming: Evolution and spreading of the 1990s warm event in the Nordic Seas and the Arctic Ocean. *J. Geophys. Res.*, *108, 3034(C2)*, doi:10.1029/2001JC001265.

Karcher, M., & Oberhuber, J. M. (2002). Pathways and modification of the upper and intermediate water of the Arctic Ocean. *J. Geophys. Res.*, *107(C6)*, doi: 10.1029/2000JC000530.

Kauker, F., Kaminski, T., Ricker, R., Toudal-Pedersen, L., Dybkjaer, G., Melsheimer, C., Eastwood, S., Sumata, H., Karcher, M., & Gerdes, R. (2015). Seasonal sea ice predictions for the Arctic based on assimilation of remotely sensed observations. *The Cryosphere Discussion*, *9*, 5521–5554.

Kimura, N., Nishimura, A., Tanaka, Y., & Yamaguchi, H. (2013). Influence of winter sea-ice motion on summer ice cover in the Arctic. *Polar Research*, *32*.

Kwok, R., & Cunningham, G. F. (2008). ICESat over Arctic sea ice: Estimation of snow depth and ice thickness. *J. Geophys. Res. Oceans*, *113(C08010)*. doi:10.1029/2008JC004753.

Kwok, R., Spreen, G., & Pang, S. (2013). Arctic sea ice circulation and drift speed: Decadal trends and ocean currents. *J. Geophys. Res. Oceans*, *118*, 2408–2425, doi:10.1002/jgrc.20191.

Large, W. G., McWilliams, J. C., & Doney, S. C. (1994). Ocean vertical mixing: A review and a model with a nonlocal boundary layer parameterization. *Rev. Geophys.*, *32(4)*, 363–403, doi:10.1029/94RG01872.

Large, W. G., & Yeager, S. G. (2009). The global climatology of an interannually varying air–sea flux data set. *Climate Dynamics*, *33*, 341–364. doi:10.1007/s00382-008-0441-3.

Latarius, K., & Quadfasel, D. (2010). Seasonal to inter-annual variability of temperature and salinity in the Greenland Sea Gyre: heat and freshwater budgets. *Tellus A*, *62*, 497–515. doi:10.1111/j.1600-0870.2010.00453.x.

Lavergne, T., Eastwood, S., Teffah, Z., Schyberg, H., & Breivik, L.-A. (2010). Sea ice motion from low-resolution satellite sensors: An alternative method and its validation in the Arctic. *J. Geophys. Res. Oceans*, *115(C10032)*. doi:10.1029/2009JC005958.

Laxon, S. W., Giles, K. A., Ridout, A. L., Wingham, D. J., Willatt, R., Cullen, R., Kwok, R., Schweiger, A., Zhang, J., Haas, C., Hendricks, S., Krishfield, R., Kurtz, N., Farrell, S., & Davidson, M. (2013). CryoSat-2 estimates of Arctic sea ice thickness and volume. *Geophys. Res. Lett.*, *40*, 732–737, doi:10.1002/grl.50193.

Lemke, P., & Manley, T. O. (1984). The seasonal variation of the mixed layer and the pycnocline under polar sea ice. *J. Geophys. Res. Oceans*, *89*, 6494–6504. doi:10.1029/JC089iC04p06494.

Losch, M., Menemenlis, D., Campin, J. M., Heimbach, P., & Hill, C. (2010). On the formulation of sea-ice models: Part 1: Effects of different solver implementations and parameterizations. *Ocean Mod.*, *33*, 129–144, doi: 10.1016/j.ocemod.2009.12.008.

Lu, P., Li, Z., Cheng, B., & Leppäranta, M. (2011). A parameterization of the ice-ocean drag coefficient. *J. Geophys. Res.*, *116, C07019*, doi:10.1029/2010C006878.

Lüpkes, C., & Birnbaum, G. (2005). Surface drag in the Arctic marginal sea-ice zone: A comparison of different parameterisation concepts. *Boundary-Layer Meteorology*, *117*, 179–211, doi: 10.1007/s10546–005–1445–8.

Lüpkes, C., & Gryanik, V. M. (2015). A stability-dependent parametrization of transfer coefficients for momentum and heat over polar sea ice to be used in climate models. *J. Geophys. Res. Atmospheres*, *120*, 552–581. doi:10.1002/2014JD022418.

Lüpkes, C., Gryanik, V. M., Hartmann, J., & Andreas, E. L. (2012). A parametrization, based on sea ice morphology, of the neutral atmospheric drag coefficients for weather prediction and climate models. *J. Geophys. Res.*, *117, D13112*, doi: 10.1029/2012JD017630.

Lüpkes, C., Gryanik, V. M., Roesel, V. M., Birnbaum, G., & Kaleschke, L. (2013). Effect of sea ice morphology during Arctic summer on atmospheric drag coefficients used in climate models. *Geophys. Res. Lett.*, *40(2)*, 446–451, doi:10.1002/grl.50081.

Marshall, J., Adcroft, A. J., Hill, C. N., Perelman, L., & Heisey, C. (1997). A finite-volume, incompressible Navier Stokes model for studies of the ocean on parallel computers. *J. Geophys. Res.*, *102(C3)*, 5753–5766, doi:10.1029/96JC02775.

Martin, T. (2006). Comparison of different ridge formation models of Arctic sea ice with observations from laser profiling. *Ann. Glaciol.*, *44*, 403–410.

Martin, T. (2007). *Arctic Sea Ice Dynamics: Drift and Ridging in Numerical Models and Observations*. Ph.D. thesis Bremen University. Berichte zur Polar- und Meeresforschung (Reports on Polar and Marine Research), Bremerhaven, Alfred Wegener Institute for Polar and Marine Research, 563, 229 p.

Martin, T., Steele, M., & Zhang, J. (2014). Seasonality and long-term trend of Arctic Ocean surface stress in a model. *Journal of Geophysical Research: Oceans*, *119*, 1723–1738. doi:10.1002/2013JC009425.

Martin, T., Tsamados, M., Schroeder, D., & Feltham, D. L. (2016). The impact of variable sea ice roughness on changes in Arctic Ocean surface stress:

A model study. *J. Geophys. Res. Oceans*, *121*, 1931–1952. doi:10.1002/2015JC011186.

Massonnet, F., Goosse, H., Fichefet, T., & Counillon, F. (2014). Calibration of sea ice dynamic parameters in an ocean-sea ice model using an ensemble Kalman filter. *Journal of Geophysical Research: Oceans*, *119*, 4168–4184. doi:10.1002/2013JC009705.

McPhee, M. G. (2008). *Air-Ice-Ocean Interaction: Turbulent Ocean Boundary Layer Exchange Processes*. Springer, Miles McPhee Research Company, Naches, Wash.

Menemenlis, D., Fukumori, I., & Lee, T. (2005). Using Green's Functions to Calibrate an Ocean General Circulation Model. *Monthly Weather Review*, *133*, 1224–1240. doi:10.1175/MWR2912.1.

Monterey, G., & deWitt, L. (1997). Seasonal variability of global mixed layer depth from WOD98 temperature and salinity profiles. *NOAA Atlas NESDIS*, *14*, 964–978. doi: 10.1034/j.1600–0870.1999.00029.x.

Nguyen, A. T., Menemenlis, D., & Kwok, R. (2011). Arctic ice-ocean simulation with optimized model parameters: Approach and assessment. *J. Geophys. Res. Oceans*, *116(C04025)*. doi:10.1029/2010JC006573.

Peralta-Ferriz, C., & Woodgate, R. A. (2015). Seasonal and interannual variability of pan-Arctic surface mixed layer properties from 1979 to 2012 from hydrographic data, and the dominance of stratification for multi-year mixed layer depth shoaling. *Progress in Oceanography*, *134*, 19–53, doi:10.1016/j.pocean.2014.12.005.

Petty, A. A., Tsamados, M. C., & Kurtz, N. T. (2017). Atmospheric form drag coefficients over Arctic sea ice using remotely sensed ice topography data, spring 2009–2015. *J. Geophys. Res. Earth Surface*, *122*, 1472–1490. doi:10.1002/2017JF004209.

Proshutinsky, A., Krishfield, R., Timmermans, M.-L., Toole, J., Carmack, E., McLaughlin, F., Williams, W. J., Zimmermann, S., Itoh, M., & Shimada, K. (2009). Beaufort Gyre freshwater reservoir: State and variability from observations. *J. Geophys. Res Oceans*, *114*. doi:10.1029/2008JC005104.

Proshutinsky, A., Steele, M., Zhang, J., Holloway, G., Steiner, N., Häkkinen, S., Holland, D. M., Gerdes, R., Köberle, C., Karcher, M., Johnson, M., Maslowsky, W., Zhang, Y., Hibler, W. D., & Wang, J. (2001). The Arctic Ocean Model Intercomparison Project (AOMIP). *EOS*, *82(51)*, 637–644.

Proshutinsky, A. Y., & Johnson, M. A. (1997). Two circulation regimes of the wind-driven Arctic Ocean. *J. Geophys. Res. Oceans*, *102*, 12493–12514. doi:10.1029/97JC00738.

Rabenstein, L., Hendricks, S., Martin, T., Pfaffhuber, A., & Haas, C. (2010). Thickness and surface-properties of different sea-ice regimes within the Arctic Trans Polar Drift: Data from summers 2001, 2004 and 2007. *J. Geophys. Res.*, *115, C12059*, doi:10.1029/2009JC005846.

Roach, L. A., Tett, S. F. B., Mineter, M. J., Yamazaki, K., & Rae, C. D. (2018). Automated parameter tuning applied to sea ice in a global climate model. *Climate Dynamics*, *50*, 51–65. doi:10.1007/s00382-017-3581-5.

Rothrock, D. A. (1975). The Energetics of the Plastic Deformation of Pack Ice by Ridging. *J. Geophys. Res.*, *80(33)*, 4514–4519, doi:10.1029/JC080i033p04514.

Rothrock, D. A., Yu, Y., & Maykut, G. A. (1999). Thinning of Arctic sea-ice cover. *Geophys. Res. Lett.*, *26(23)*, 3469–3472, doi: 10.1029/1999GL010863.

Roy, F., Chevallier, M., Smith, G. C., Dupont, F., Garric, G., Lemieux, J.-F., Lu, Y., & Davidson, F. (2015). Arctic sea ice and freshwater sensitivity to the treatment of the atmosphere-ice-ocean surface layer. *J. Geophys. Res. Oceans*, *120*, 4392–4417, doi:10.1002/ 2014JC010677.

Rudels, B., Björk, G., Nilsson, J., Winsor, P., Lake, I., & Nohr, C. (2005). The interaction between waters from the Arctic Ocean and the Nordic Seas

north of Fram Strait and along the East Greenland Current: results from the Arctic Ocean-02 Oden expedition. *Journal of Marine Systems*, *55*, 1–30. doi:10.1016/j.jmarsys.2004.06.008.

Rudels, B., Friedrich, H. J., & Quadfasel, D. (1999). The Arctic Circumpolar Boundary Current. *Deep-Sea Res. Part II: Topical Studies in Oceanography*, *46*, 1023–1062.

Rudels, B., Jones, E. P., Anderson, L. G., & Kattner, G. (1994). On the intermediate Depth Waters of the Arctic Ocean. In O. M. Johannessen, R. D. Muench, & J. E. Overland (Eds.), *The Polar Oceans and Their Role in shaping the Global Climate: The Nansen Centennial Volume* (pp. 33–46). Washington: American Geophysical Union.

Saha, S., Moorthi, S., Wu, X., Wang, J., Nadiga, S., Tripp, P., Behringer, D., Hou, Y.-T., Chuang, H.-y., Iredell, M., Ek, M., Meng, J., Yang, R., Mendez, M. P., van den Dool, H., Zhang, Q., Wang, W., Chen, M., & Becker, E. (2014). The NCEP Climate Forecast System Version 2. *Journal of Climate*, *27*, 2185–2208. doi:10.1175/JCLI-D-12-00823.1.

Semtner, A. J. (1976). A Model for the Thermodynamic Growth of Sea Ice in Numerical Investigations of Climate. *Journal of Physical Oceanography*, *6*, 379–389. doi:10.1175/1520-0485(1976)006<0379:AMFTTG>2.0.CO;2.

Serreze, M. C., Holland, M. M., & Stroeve, J. (2007). Perspectives on the Arctic's Shrinking Sea-Ice Cover. *Science*, *315(5818)*, 1533–1536, doi: 10.1126/science.1139426.

Serreze, M. C., Maslanik, J. A., Scambos, T. A., Fetterer, F., Stroeve, J., Knowles, K., Fowler, C., Drobot, S., Barry, R. G., & Haran, T. M. (2003). A record minimum Arctic sea ice extent and area in 2002. *Geophys. Res. Lett.*, *30(1110)*, doi:10.1029/2002GL016406.

Shaw, W. J., Stanton, T. P., McPhee, M. G., & Kikuchi, T. (2008). Estimates

of surface roughness length in heterogeneous under-ice boundary layers. *J. Geophys. Res.*, *113(C08030)*, doi:10.1029/2007JC004550.

Shirasawa, K. (1986). Water stress and ocean current measurements under first?year sea ice in the Canadian Arctic. *J. Geophys. Res. Oceans*, *91*, 14305–14316. doi:10.1029/JC091iC12p14305.

Shirasawa, K., & Aota, M. (1991). Atmospheric boundary layer measurements over sea ice in the Sea of Okhotsk. *J. Mar. Syst.*, *2*, 63–79, doi:10.1016/0924–7963(91)90014–L.

Shirasawa, K., & Ingram, R. G. (1991). Characteristics of the turbulent oceanic boundary layer under sea ice. Part 1: A review of the ice-ocean boundary layer. *J. Mar. Syst.*, *2(1)*, 153–160, doi:10.1016/0924–7963(91)90021–L.

Spreen, G., Kwok, R., & Menemenlis, D. (2011). Trends in Arctic sea ice drift and role of wind forcing: 1992-2009. *Geophys. Res. Lett.*, *38, L19501*, doi:10.1029/2011GL048970.

Steele, M., Morison, J. H., & Untersteiner, N. (1989). The partition of air-ice-ocean momentum exchange as a function of ice concentration, floe size, and draft. *J. Geophys. Res.*, *94(C9)*, 12739–12750, doi:10.1029/JC094iC09p12739.

Steiner, N. (2001). Introduction of variable drag coefficients into sea-ice models. *Annals of Glaciology*, *33(1)*, 181–186, doi:10.3189/172756401781818149.

Steiner, N., Harder, M., & Lemke, P. (1999). Sea-ice roughness and drag coefficients in a dynamic-thermodynamic sea-ice model for the Arctic. *Tellus*, *A, 51*, 964–978. doi: 10.1034/j.1600–0870.1999.00029.x.

Steiner, N., Holloway, G., Gerdes, R., Häkkinen, S., Holland, D., Karcher, M., Kauker, F., Maslowski, W., Proshutinsky, A., Steele, M., & Zhang, J. (2004). Comparing modeled streamfunction, heat and freshwater content in the Arctic Ocean. *Ocean Modelling*, *6*, 265–284. doi:10.1016/S1463-5003(03)00013-1.

Stroeve, J., Barrett, A., Serreze, M., & Schweiger, A. (2014). Using records from submarine, aircraft and satellites to evaluate climate model simulations of Arctic sea ice thickness. *The Cryosphere*, *8*, 1839–1854. doi:10.5194/tc-8-1839-2014.

Stroeve, J. C., Holland, M. M., Meier, W., Scambos, T., & Serreze, M. (2007). Arctic sea ice decline: Faster than forecast. *Geophys. Res. Lett.*, *34, L09501*, doi:10.1029/2007GL029703.

Stroeve, J. C., Kattsov, V., Barret, P., Serreze, M., Pavlova, T., Holland, M., & Meier, W. N. (2012a). Trends in Arctic sea ice extent from CMIP5, CMIP3 and observations. *Geophys. Res. Lett.*, *39, L16502*, doi:10.1029/2012GL052676.

Stroeve, J. C., Serreze, M. C., Holland, M. M., Kay, J. E., Malanik, J., & Barret, A. P. (2012b). The Arctic's rapidly shrinking sea ice cover: a research synthesis. *Climatic Change*, *110(3-4)*, 1005–1027.

Sumata, H., Kwok, R., Gerdes, R., Kauker, F., & Karcher, M. (2015). Uncertainty of Arctic summer ice drift assessed by high-resolution SAR data. *J. Geophys. Res. Oceans*, *120*, 5285–5301. doi:10.1002/2015JC010810.

Sumata, H., Lavergne, T., Girard-Ardhuin, F., Kimura, N., Tschudi, M. A., Kauker, F., Karcher, M., & Gerdes, R. (2014). An intercomparison of Arctic ice drift products to deduce uncertainty estimates. *J. Geophys. Res. Oceans*, *119*, 4887–4921. doi:10.1002/2013JC009724.

Swift, J. H., Jones, E. P., Carmack, E. C., Hingstone, M., Macdonald, R. W., McLaughlin, F. A., & Perkin, R. G. (1997). Waters of the Makarov and Canada Basins. *Deep-Sea Res. Part II: Topical Studies in Oceanography*, *44*, 1503–1529, doi: 10.1016/s0967–0645(97)00055–6.

Treshnikov, A., & Baranov, G. (1973). *Water Circulation in the Arctic Basin*. Israel Program For Scientific Translations Catalog.

Tsamados, M., Felthams, D. L., Schroeder, D., Flocco, D., Farrell, S. L., Kurtz, N., Laxon, S. W., & Bacon, S. (2014). Impact of variable atmospheric and oceanic form drag on simulations of Arctic sea ice. *J. Phys. Oceanogr.*, *44*, 1329–1353.

Ungermann, M., Tremblay, L. B., Martin, T., & Losch, M. (2017). Impact of the ice strength formulation on the performance of a sea ice thickness distribution model in the Arctic. *J. Geophys. Res. Oceans*, *122*, 2090–2107. doi:10.1002/2016JC012128.

Wamser, C., & Martinson, D. G. (1993). Drag coefficients for winter Antarctic pack ice. *J. Geophys. Res.*, *98(C7)*, 12431–12437.

Yang, J., Comiso, J., Walsh, D., Krishfield, R., & Honjo, S. (2004). Storm-driven mixing and potential impact on the Arctic Ocean. *J. Geophys. Res. Oceans*, *109*. doi:10.1029/2001JC001248.

Table 1: Range of observed, estimated from topography data, and modeled values for atmospheric and oceanic drag coefficients taken from literature. Values reported are for the Arctic Ocean and for regions of interest (see also Figure 1): Lincoln Sea (LS), Beaufort Sea (BS), and Central Arctic (CA).

	Atmospheric (10^{-3})				Oceanic (10^{-3})
Source	range	LS	BS	CA	range
Observations					
Guest & Davidson (1991)	0.61 - 9.1	-	-	-	-
Lu et al. (2011)	-	-	-	-	1.05 - 22.28
Topography-based Estimations					
Castellani et al. (2014)	0.88 - 4.66	2.59	1.65	1.65	-
Petty et al. (2017)	1.64 - 2.36	-	1.80	2.20	-
Model results					
Tsamados et al. (2014)	0.4 - 4	-	-	-	2 - 20

Table 2: Values of the parameters entering equations (10) and (11) for the atmospheric and oceanic drag coefficients in the original formulation from Steiner (2001), and for the optimized run referred to as DRAGS run.

	m_a	m_w	d_a	d_w
Steiner (2001)	1.9×10^{-8}	6×10^{-8}	1.3×10^{-3}	2.6×10^{-3}
DRAGS	0.90423×10^{-8}	3.1226×10^{-8}	1.2839×10^{-3}	2.66110^{-3}

Table 3: Cost function values for the run with original parameters from Steiner (2001), the DRAGS and MEAN runs, and the CTRL run with constant values of oceanic and atmospheric drag coefficients from Castro-Morales et al. (2014). The cost function is computed for ice concentration A and ice drift $|\vec{v}|$, in summer (S) and winter (W), and ice thickness H_i in March (M) and November (N).

	A S	A W	H_i M	H_i N	$\|\vec{v}\|$ S	$\|\vec{v}\|$ W	Sum
Steiner (2001)	1.06	1.32	0.38	0.39	1.01	1.73	5.89
DRAGS	1.12	1.44	0.38	0.34	0.48	0.91	4.67
MEAN	1.16	1.49	0.40	0.33	0.51	0.81	4.70
CTRL	1.21	1.32	0.49	0.35	0.62	0.95	4.94

Table 4: Minimum, maximum, mean, and median values of atmospheric and oceanic drag coefficients obtained with the DRAGS run. The last column shows the values of the coefficients used in the CTRL run.

	min (10^{-3})	max (10^{-3})	mean (10^{-3})	median (10^{-3})	CTRL (10^{-3})
c_a	0.8	4.6	1.36	1.27	1
c_w	1.2	13.6	2.82	2.63	5.4

Table 5: Mean (with one standard deviation) and maximum values of atmospheric and oceanic drag coefficients in March (M) and September (S) of the climatological year of the DRAGS run. Values presented are for the entire Arctic Basin (AB) and for the regions of interest (Figure 1).

	mean $c_a(10^{-3})$	max $c_a(10^{-3})$	mean $c_w(10^{-3})$	max $c_w(10^{-3})$
AB (M)	1.23 (0.32)	3.66	2.50 (1.06)	11.02
AB (S)	1.68 (0.52)	3.34	3.56 (1.52)	9.24
LS (M)	1.66 (0.84)	3.12	4.15 (2.88)	9.17
LS (S)	1.86 (0.91)	3.27	4.53 (2.88)	9.20
BS (M)	1.35 (0.12)	1.74	3.06 (0.42)	4.40
BS (S)	1.83 (0.39)	2.42	4.03 (1.10)	5.91
CA (M)	1.33 (0.12)	2.14	3.02 (0.40)	5.65
CA (S)	1.92 (0.21)	2.86	4.23 (0.61)	7.22
ESS (M)	1.19 (0.08)	1.89	2.50 (0.28)	4.72
ESS (S)	1.64 (0.36)	2.16	3.31 (0.89)	4.60
LapS (M)	0.97 (0.05)	1.31	1.74 (0.16)	2.68
LapS (S)	1.54 (0.24)	1.96	2.92 (0.58)	3.92

Table 6: Mean and maximum values of the atmospheric surface length z_0 for the entire Arctic Basin (AB) and for the regions of interest (Figure 1). The brackets contain the value from Guest & Davidson (1991), their Table 1, closest to our computed value and the corresponding sea-ice category.

	mean $z_0\,(10^{-3})$	max $z_0\,(10^{-3})$
AB	0.53 (0.33 - FYI/MYI very smooth)	27.4 (27.0 - MYI very rough)
LS	2.30 (2.0 - MYI smooth)	17.9 (10.0 - MYI rough)
BS	0.59 (0.33 - FYI/MYI very smooth)	3.81 (7.5 - FYI rough)
CA	0.47 (0.33 - FYI/MYI very smooth)	2.30 (2.0 - MYI smooth)
ESS	0.40 (0.33 - FYI/MYI very smooth)	3.20 (2.0 - MYI smooth)
LapS	0.22 (0.33 - FYI/MYI very smooth)	1.67 (1.3 - FYI smooth)

Table 7: Mean values (with one standard deviation) of sea-ice concentration A, sea-ice thickness H_i (m), sea-ice drift $|\vec{v}|$ (cm s^{-1}) and sea surface temperature θ ($^\circ C$) in September for the DRAGS run (A), the MEAN run (B) and the CTRL run (C). The colors of the cells for the DRAGS run indicate whether the number is larger (red) or smaller (blue) than in the MEAN run. The same holds for the colors of the cells of the MEAN run, but in this case the difference is calculated with respect to the CTRL run.

A	DRAGS					
	AB	LS	BS	CA	ESS	LapS
$\bar{A}$	0.505 (0.326)	0.930 (0.048)	0.514 (0.267)	0.808 (0.036	0.371 (0.176)	0.385 (0.137)
$\bar{H_i}$	1.00 (1.08)	6.62 (4.10)	0.98 (0.60)	1.48 (0.18)	0.56 (0.28)	0.50 (0.21)
$\overline{\|\vec{v}\|}$	6.64 (5.65)	0.60 (0.65)	5.25 (2.97)	2.72 (0.4)	1.68 (0.81)	3.86 (1.07)
$\bar{\theta}$	-0.54 (1.52)	-1.66 (0.02)	-0.42 (1.24)	-1.64 (0.02)	-0.24 (0.92)	-0.77 (0.61)
B	MEAN					
	AB	LS	BS	CA	ESS	LapS
$\bar{A}$	0.511 (0.326)	0.958 (0.027)	0.508 (0.262)	0.818 (0.034)	0.391 (0.175)	0.394 (0.141)
$\bar{H_i}$	1.05 (1.16)	7.86 (3.57)	0.98 (0.61)	1.56 (0.21)	0.60 (0.28)	0.52 (0.22)
$\overline{\|\vec{v}\|}$	6.22 (5.30)	0.11 (0.23)	4.90 (2.55)	2.43 (0.34)	1.57 (0.83)	3.59 (0.94)
$\bar{\theta}$	-0.54 (1.54)	-1.68 (0.01)	-0.39 (1.26)	-1.64 (0.02)	-0.30 (0.90)	-0.76 (0.66)
C	CTRL					
	AB	LS	BS	CA	ESS	LapS
$\bar{A}$	0.329 (0.557)	0.970 (0.017)	0.519 (0.272)	0.854 (0.024)	0.477 (0.195)	0.519 (0.138)
$\bar{H_i}$	1.26 (1.27)	8.46 (3.19)	1.00 (0.66)	1.96 (0.21)	0.77 (0.36)	0.78 (0.28)
$\overline{\|\vec{v}\|}$	5.15 (4.77)	0.02 (0.08)	3.19 (1.92)	1.58 (0.17)	1.30 (0.66)	2.84 (0.83)
$\bar{\theta}$	-0.71 (1.38)	-1.68 (0.01)	-0.49 (1.16)	-1.164 (0.02)	-0.56 (0.76)	1.05 (0.52)

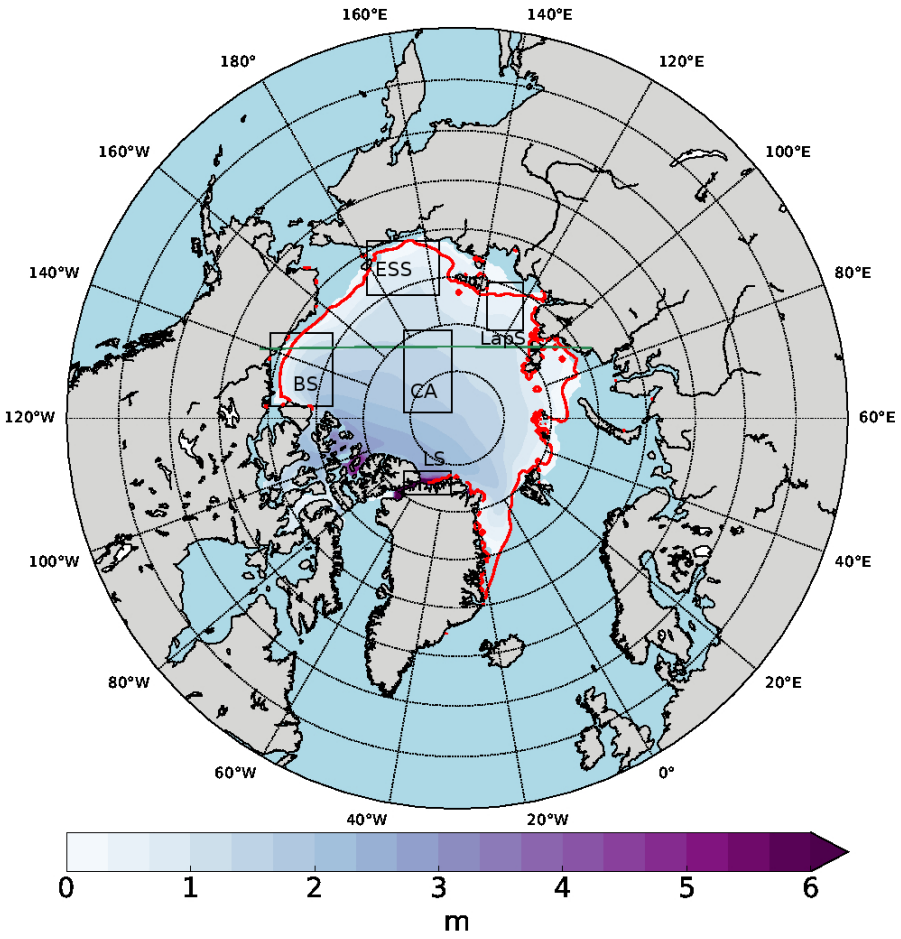

Figure 1: Map of the model domain with in colors the 1990-2010 September climatology for ice thickness (masked for ice concentration <15%) obtained with the DRAGS run. The black boxes represent the regions that are relevant in this study: Lincoln Sea (LS), Central Arctic (CA), Beaufort Sea (BS), East-Siberian Sea (ESS), and Laptev Sea (LapS). The green line represents the oceanic transect crossing the Beaufort Sea. The red contour shows the ice edge (ice concentration threshold set to 15%) from observations (EUMETSAT, Ocean and Sea Ice Satellite Application Facility, 2011). For clarity, no contour lines are drawn in the Canadian Arctic Archipelago.

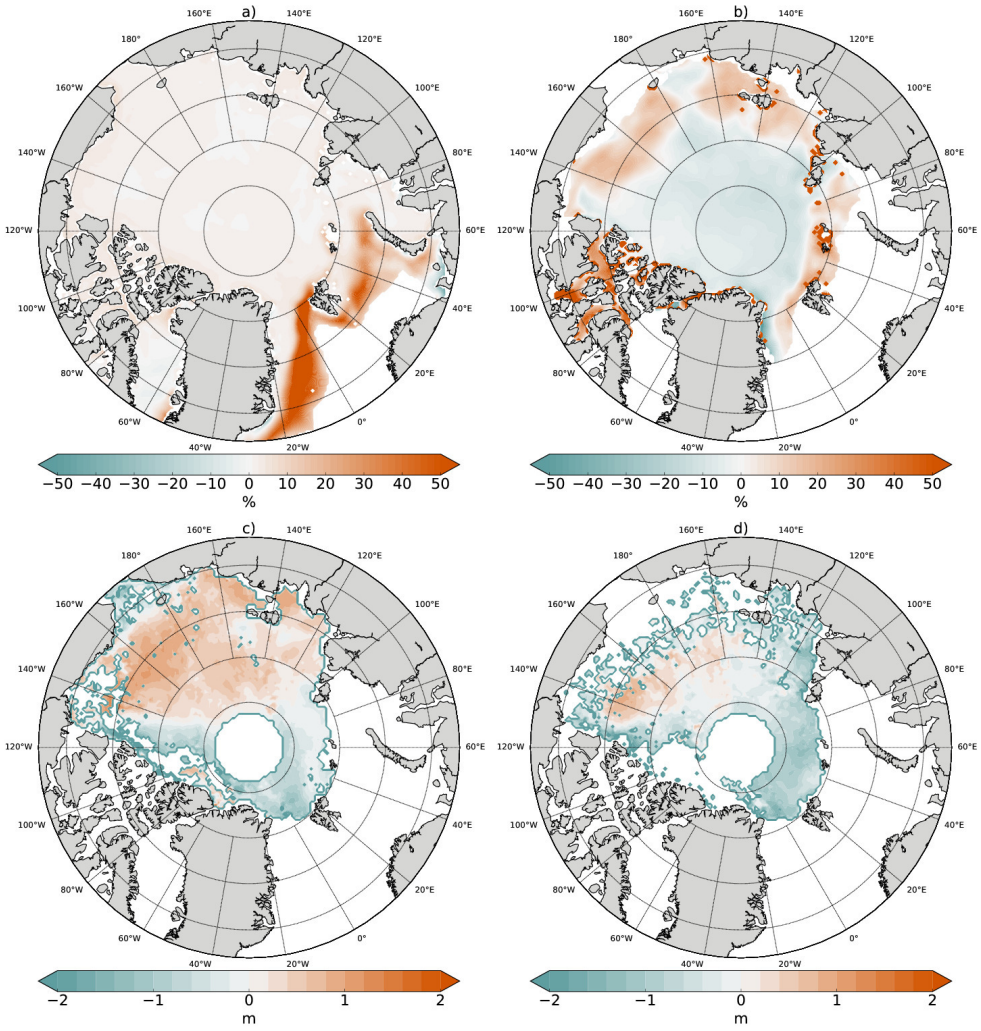

Figure 2: Ice concentration differences between the DRAGS run and OSISAF observations (EUMETSAT, Ocean and Sea Ice Satellite Application Facility, 2011) in a) March and b) September. Ice thickness differences between the DRAGS run and ICESat observations (Kwok & Cunningham, 2008) in c) March and d) November. Ice concentration fields are masked for modeled ice concentration <15%, ice thickness from ICESat is masked for uncertainties larger than 1 m.

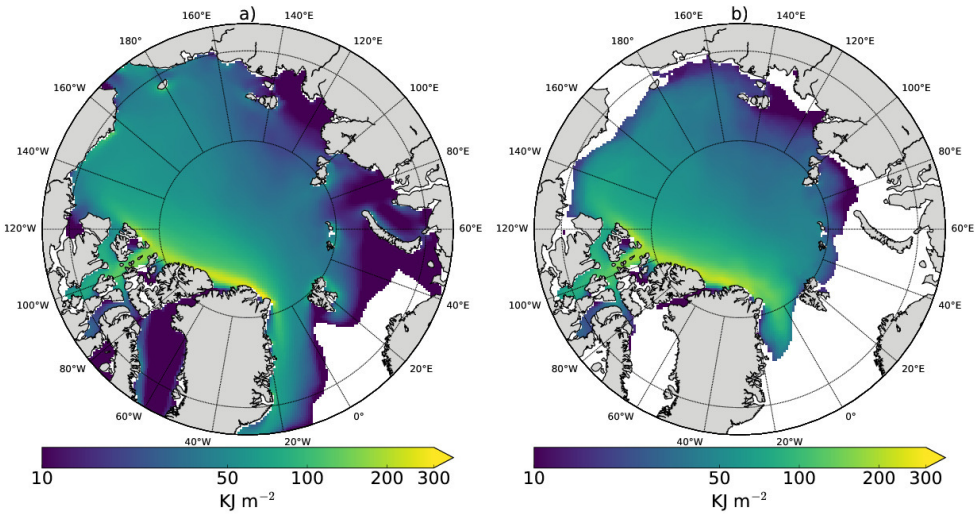

Figure 3: March (a) and September (b) climatologies (1990-2010) of deformation energy masked for ice concentration <15%.

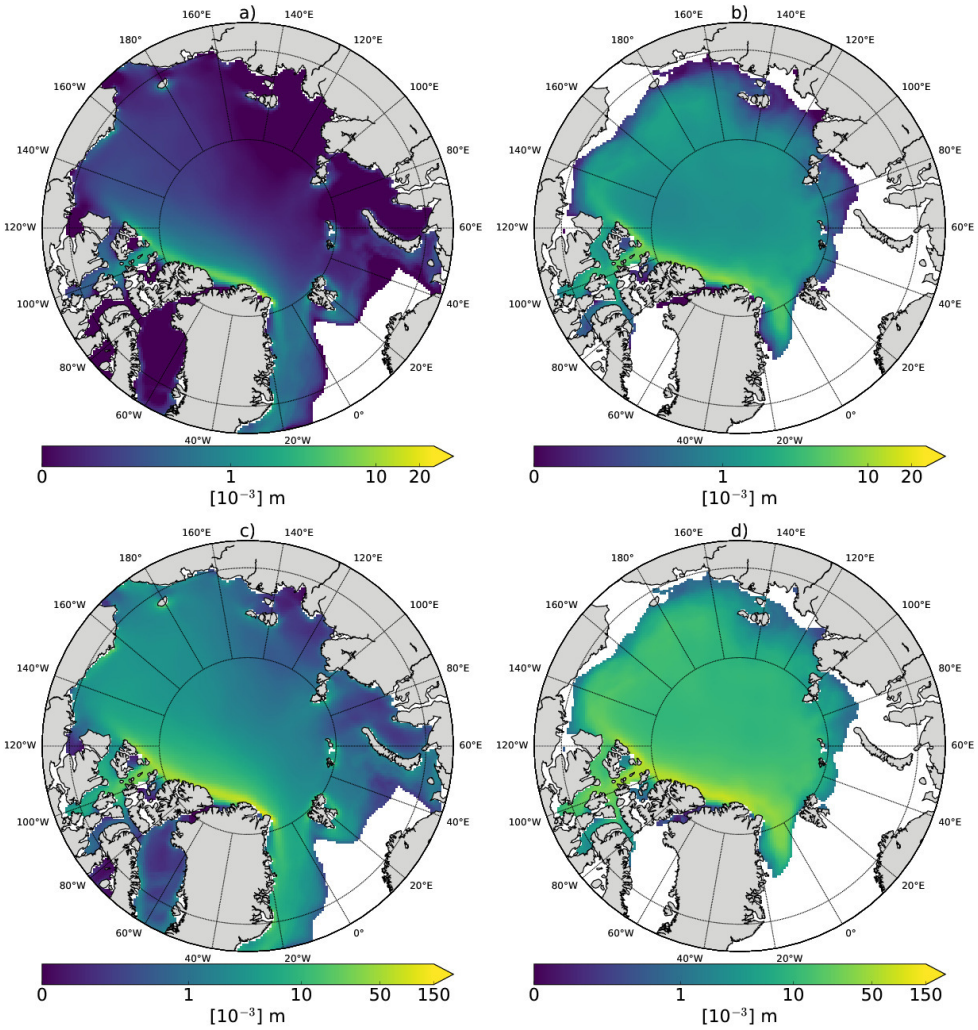

Figure 4: March (left column) and September (right column) maps of roughness length z_0 estimated from the climatologies (1990-2010) of the atmospheric (a-b) drag coefficients and oceanic (c-d) drag coefficients. The fields are masked for ice concentration <15%.

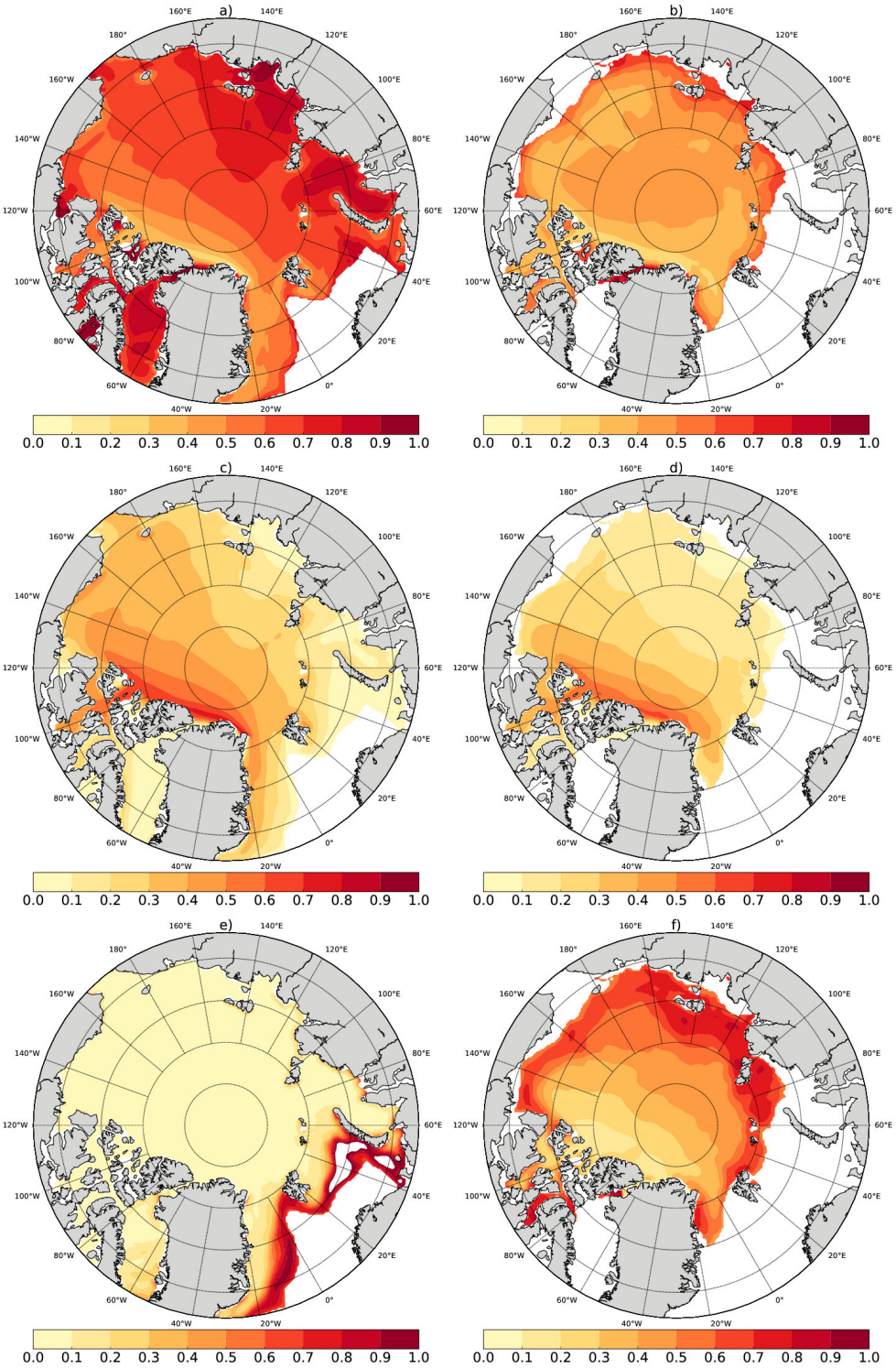

Figure 5: March (left column) and September (right column) contribution of the different terms in equation (10) to the total atmospheric drag coefficient computed as ratio over total atmospheric drag of skin drag term (a-b), deformation energy term (c-d), and ice concentration term (e-f). The fields are masked for ice concentration <15%.

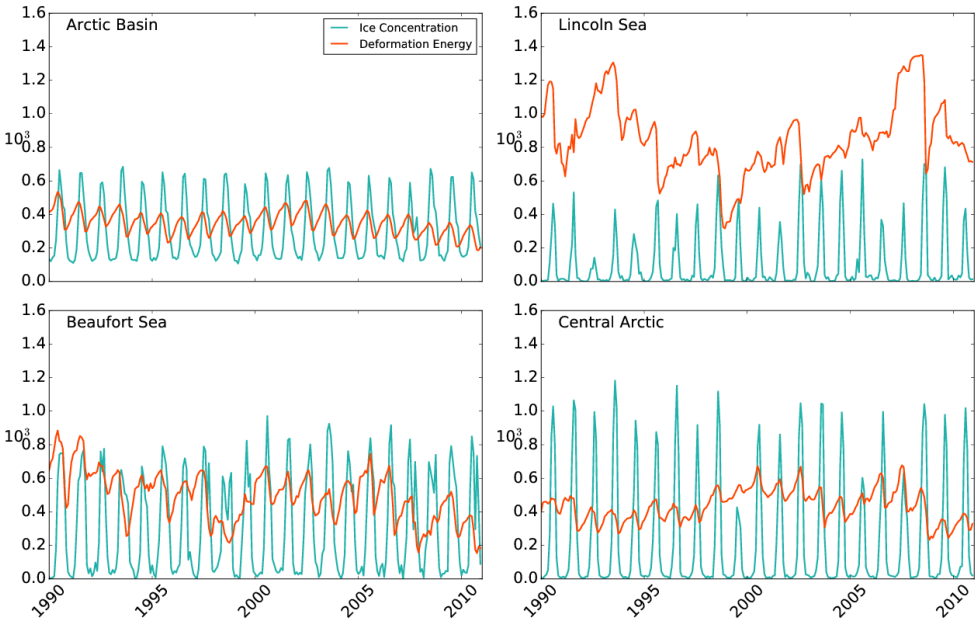

Figure 6: Monthly means of the contribution to atmospheric drag coefficients of deformation energy term (orange line) and ice concentration term (light-blue line) entering equation (10) for the entire Arctic Basin and for some of the regions highlighted in Figure 1.

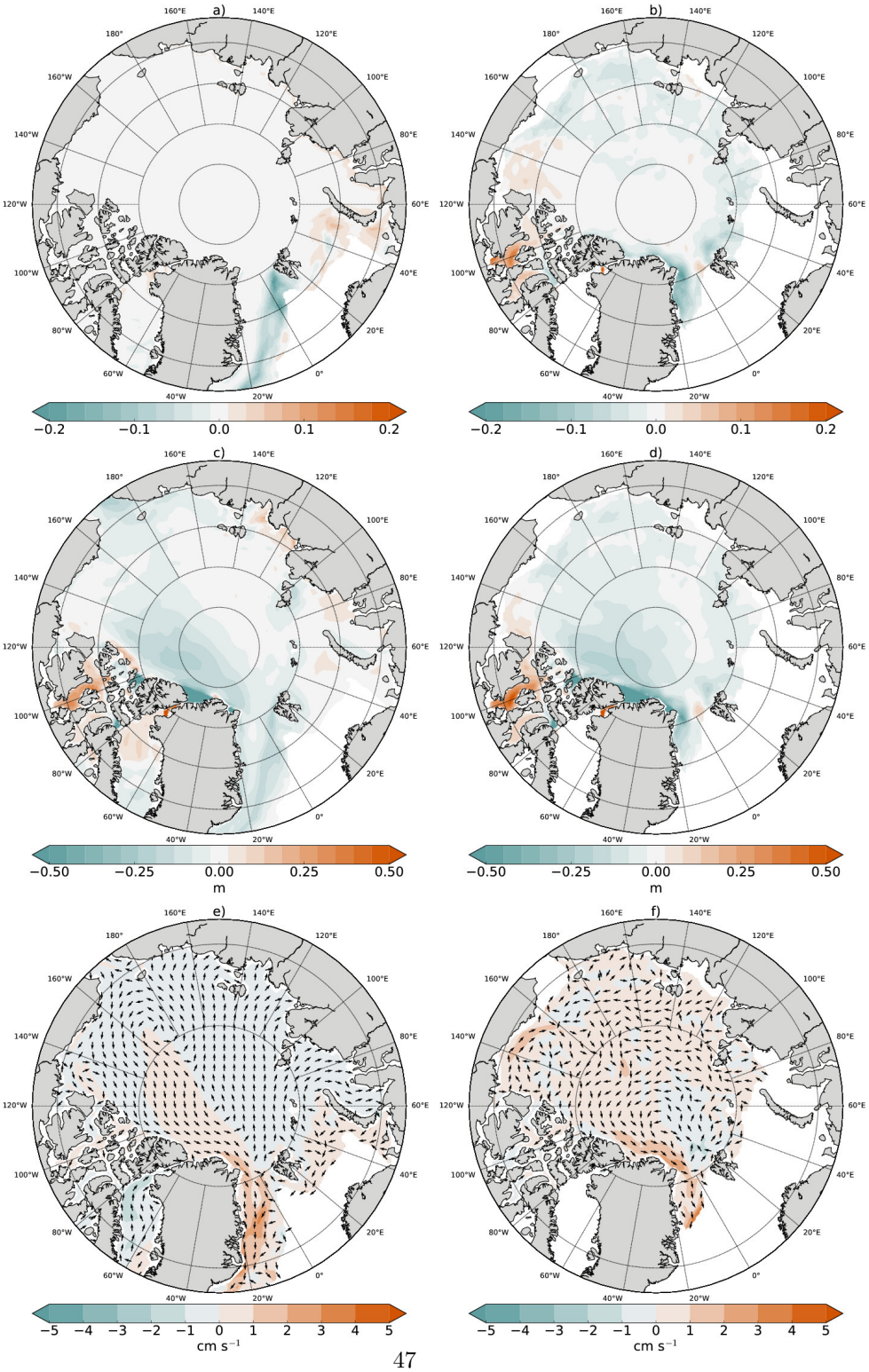

Figure 7: Differences DRAGS - MEAN in March (left column) and September (right column) 1990-2010 climatologies for sea-ice concentration (a-b), thickness (c-d) and drift (e-f). Ice concentration and ice thickness are masked for ice concentration <15% in the DRAGS run, ice drift is masked for thickness <10 cm.

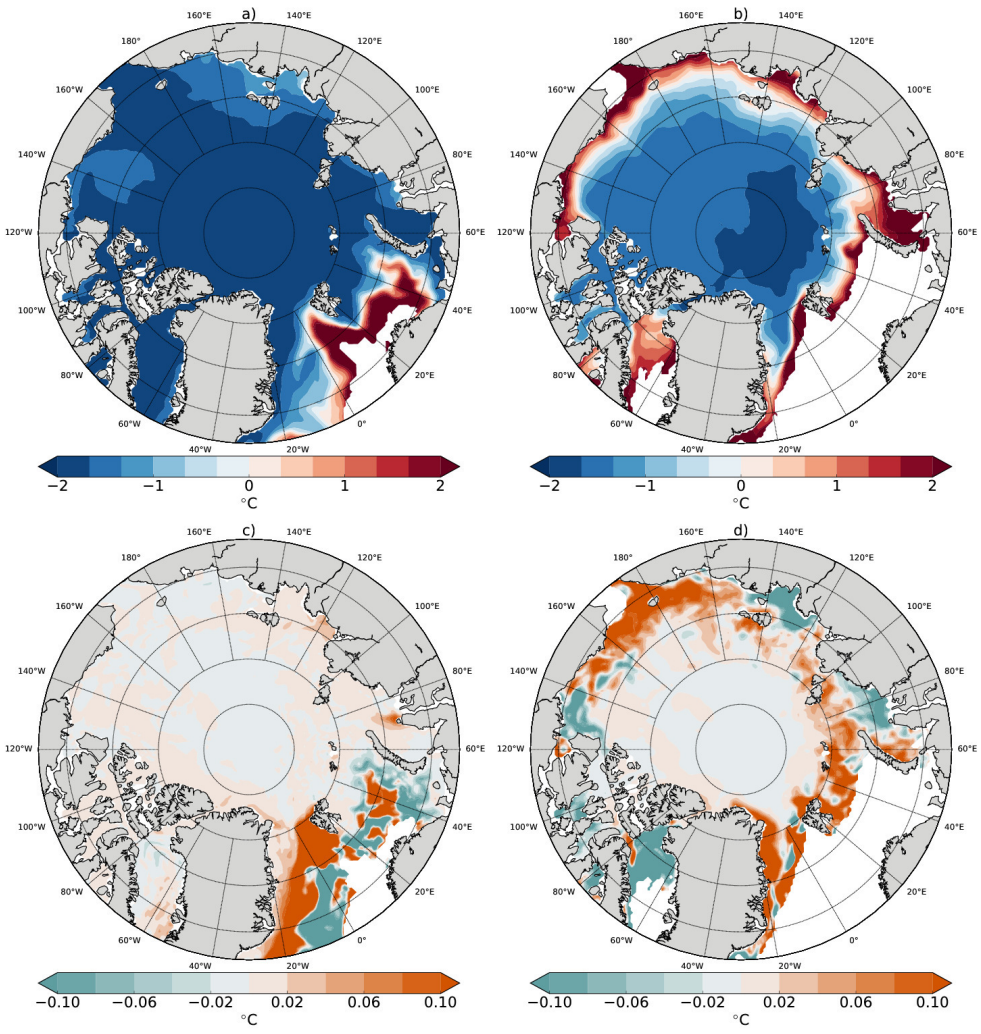

Figure 8: March (left column) and September (right column) sea surface temperatures for the DRAGS run (a-b) and for differences DRAGS - MEAN (c-d). The fields are masked in open water.

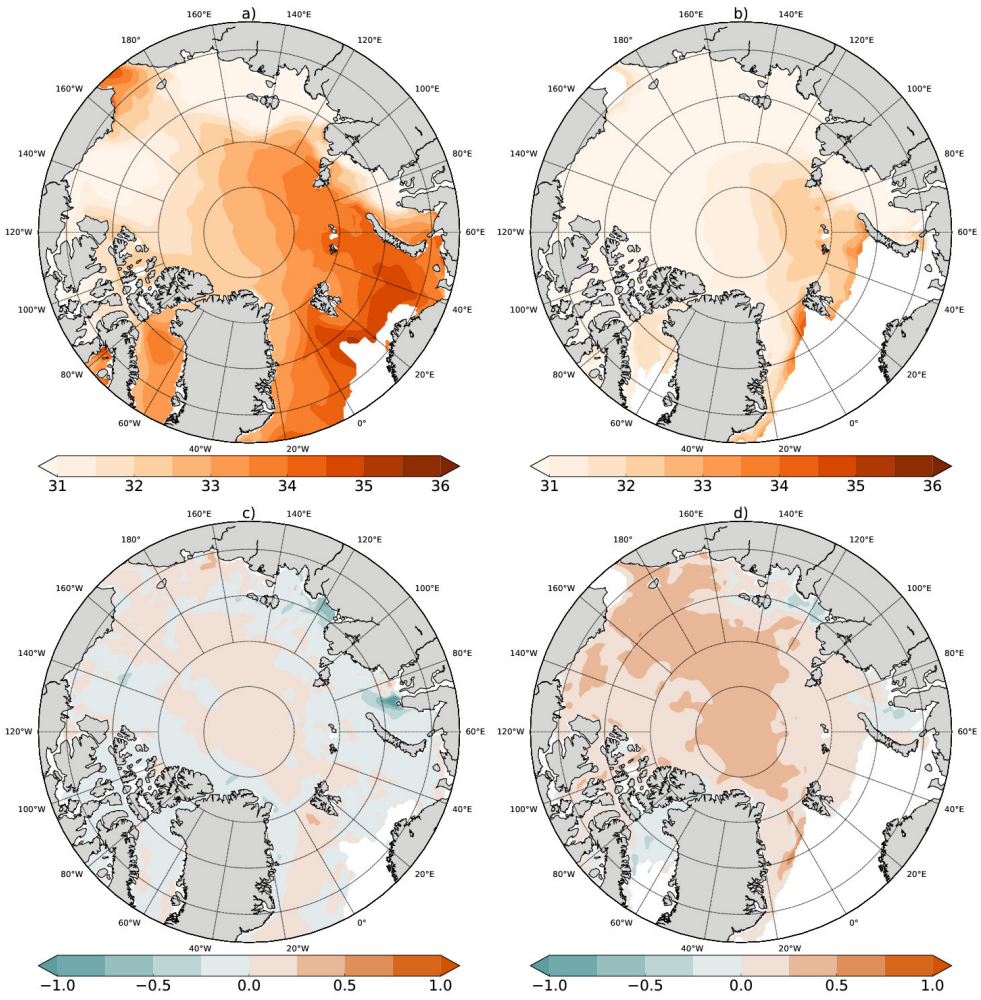

Figure 9: March (left column) and September (right column) surface salinity for the DRAGS run (a-b) and for differences DRAGS - MEAN (c-d). The fields are masked in open water.

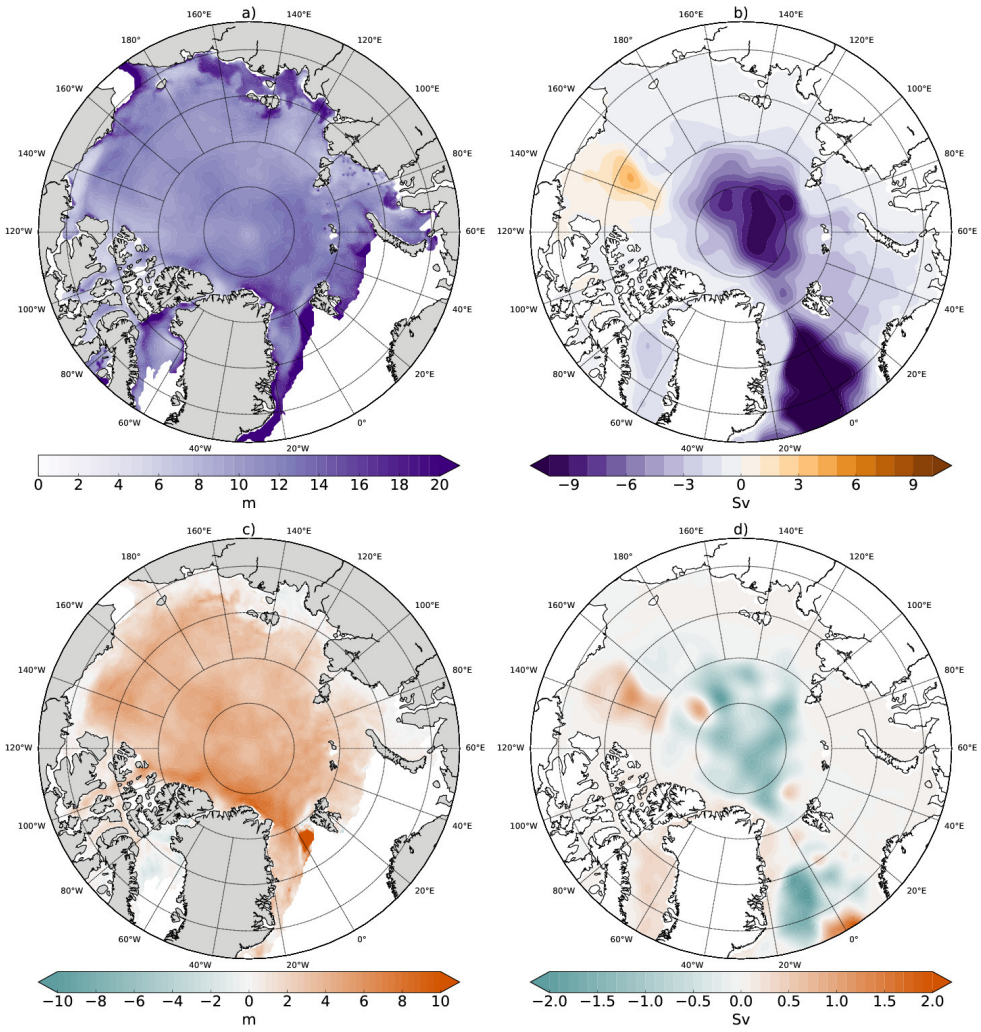

Figure 10: September climatologies of mixed layer depth (left column) masked in open water and stream function (right column) in DRAGS (a-b), and differences DRAGS - MEAN (c-d).

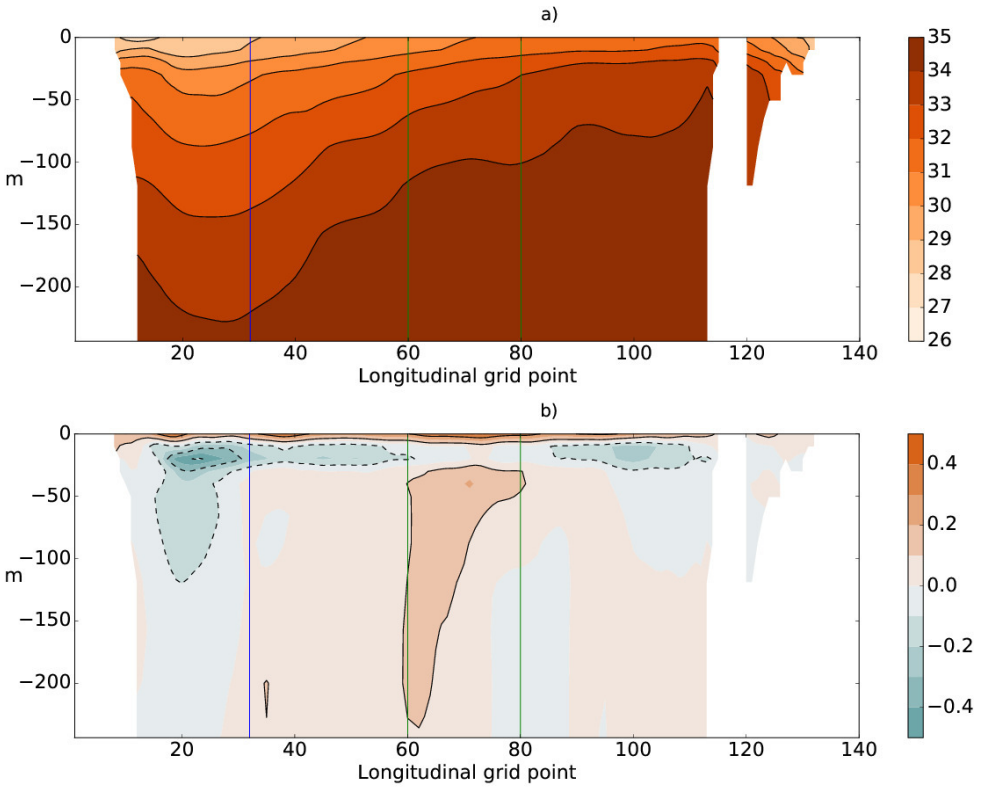

Figure 11: Salinity vertical profile in September along an oceanic transect passing through the Beaufort Sea (Figure 1) for the DRAGS run (a), and differences in salinity vertical profile (b) between DRAGS and MEAN. The blue line represents the right border of the BS region, the green lines enclose the CA region.

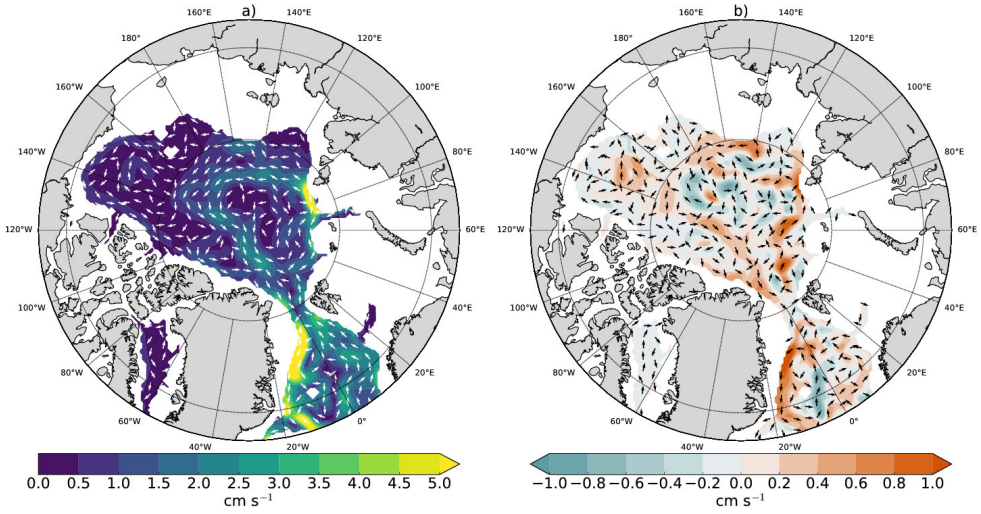

Figure 12: Mid-AW circulation in September in the DRAGS run (a), and differences DRAGS - MEAN (b).

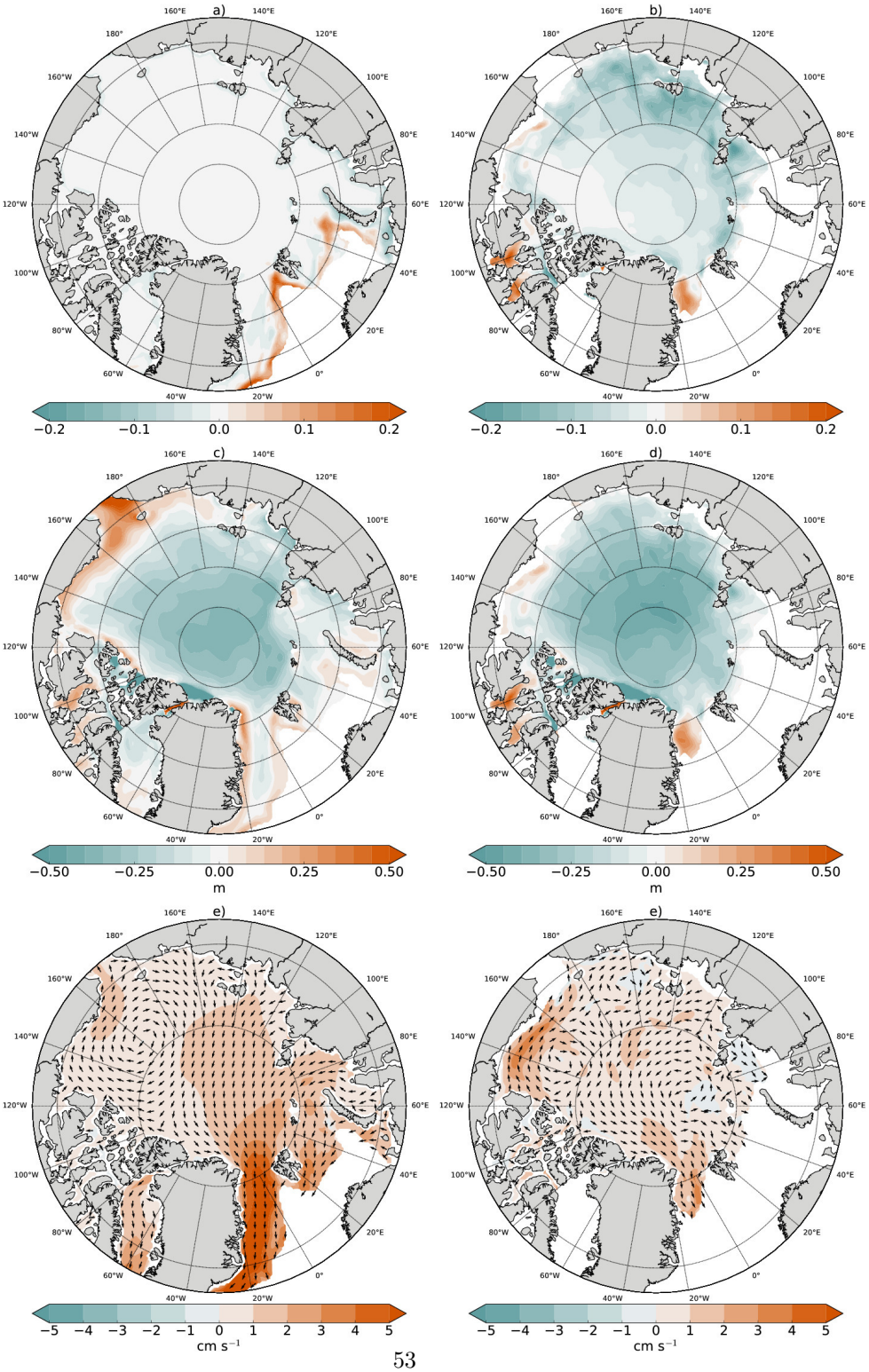

Figure 13: Differences MEAN-CTRL in March (left column) and September (right column) for ice concentration (a-b), thickness (c-d) and drift (e-f). Ice concentration and ice thickness are masked for ice concentration <15% in the MEAN run, ice drift is masked for thickness <10 cm.